

1 **Early Jurassic climate and atmospheric CO₂ concentration in the**
2 **Sichuan paleobasin, Southwest China**

3
4 Xianghui Li¹, Jingyu Wang¹, Troy Rasbury², Min Zhou¹, Zhen Wei¹, Chaokai Zhang¹

5 ¹State Key Laboratory for Mineral Deposits Research, School of Earth Sciences and Engineering, Nanjing University,
6 Nanjing 210023 China.

7 ²Department of Geosciences, Stony Brook University, Stony Brook, NY 11794-2100, USA

8 *Correpondence to:* Xiangui Li (leeschhui@126.com)

9

10 **Abstract:** Climatic oscillations had been developed through the (Early) Jurassic from marine sedimentary archives, but
11 remain unclear from terrestrial records. This work presents investigation of climate-sensitive sediments and carbon and
12 oxygen isotope analyses of lacustrine and pedogenic carbonates for the Early Jurassic Ziliujing Formation from the grand
13 Sichuan paleobasin (GSB), Southwest China. Sedimentary and stable isotope proxies manifest that an overall secular (semi-)
14 arid climate dominated the GSB during the Early Jurassic except for the Hettangian. This climate pattern is similar to the
15 arid climate in the Colorado Plateau region, western North America, but distinct from the relatively warm-humid climate in
16 North China and high latitude in Southern Hemisphere. The estimated atmospheric CO₂ concentration (*p*CO₂) from carbon
17 isotopes of pedogenic carbonates shows a range of 980-2610 ppmV (~ 3.5-10 times the pre-industrial value) with a mean of
18 1660 ppmV. Three phases of *p*CO₂ (the Sinemurian 1500-2000 ppmV, the Pliensbachian 1000-1500 ppmV, and the early
19 Toarcian 1094-2610 ppmV) and two events of rapid falling *p*CO₂ by ~1000-1300 ppmV are observed, illustrating the *p*CO₂
20 perturbation in the Early Jurassic. The perturbation of *p*CO₂ is compatible with seawater temperature and carbon cycle from
21 the coeval marine sediments, suggesting a positive feedback of climate to *p*CO₂ through the Early Jurassic.

22

23 1. Introduction

24 Global paleotemperatures were possibly 5-10°C higher than present during the Jurassic period based on climate modelling
25 results (e.g., Rees et al., 1999; Sellwood and Valdes, 2008). However, seawater temperature fluctuated by -5 °C to +5 °C, or
26 even much higher magnitude (e.g., Suan et al., 2008; Littler et al., 2010), based on estimates from the oxygen isotopes of the
27 belemnite and bivalve fossils (Dera et al., 2011, and references therein). In the Sinemurian–Pliensbachian age, the mean sea
28 surface temperatures of the North Atlantic were in excess of 28°C (TEX₈₆), comparable with similar palaeolatitudes during
29 the Cretaceous and Early Cenozoic (Robinson et al., 2017); whereas in the late Pliensbachian age, the northern West Tethys
30 Ocean (e.g., Paris basin, northern Spain basin) was ~12.7°C (e.g., Gómez et al., 2008; Gómez and Goy, 2011; Arabas et al.,
31 2017), leading to a polar icesheet hypothesis (e.g., Sellwood and Valdes, 2008; Suan et al., 2010; Dera et al., 2011; Gómez et
32 al., 2015). At ~183 Ma of the early Toarcian oceanic anoxia event (T-OAE), the surface seawater temperature was high to
33 ~35°C (e.g., Bailey et al., 2003; Korte et al., 2015), and a high temperature (plateau) even continued in the whole Toarcian
34 (Dera et al., 2011). Examples of seawater temperature transitions between cold and hot show the climate oscillation through
35 the Early Jurassic.

36 Data from the terrestrial realm also provide important details of environmental and climatic change (e.g., Hesselbo et al.,
37 2000; Suan et al., 2010; Jenkyns, 2010; Philippe et al., 2017), from which the oscillated climate could be observed and
38 revealed too. Terrestrial proxies, such as flora (e.g., Riding et al., 2013; Deng et al., 2017; Philippe et al., 2017), vegetation
39 (Pole, 2009), and geochemistry (e.g., Riding et al., 2013; Kenny, 2015; Tramoy et al., 2016) as well as the *p*CO₂ record (e.g.,
40 Retallack, 2001a; Beerling and Royer, 2002; McElwain et al., 2005; Berner, 2006; Steinthorsdottir and Vajda, 2015) provide
41 an emerging record of the Early Jurassic terrestrial climate and environment changes. Correspondingly, the proxy application
42 of terrestrial sedimentary archives could play a key role in the global Early Jurassic correlation of the marine and terrestrial
43 climate.

44 Proxies for *p*CO₂ are the important linkage between the marine and terrestrial climatic condition. Studies of the terrestrial
45 *p*CO₂ record have focused on the Triassic-Jurassic boundary (e.g., Tanner et al., 2001; Cleveland et al., 2008; Schaller et al.,
46 2011; Steinthorsdottir and Vajda, 2015) and the Toarcian oceanic anoxic event (McElwain et al., 2005), where *p*CO₂
47 estimates range 1000 ppm to 4000 ppmV (e.g., Tanner et al., 2001; Cleveland et al., 2008; Schaller et al., 2011). Few
48 relatively continuous *p*CO₂ records and coupled terrestrial climate changes have been documented for the Early Jurassic.

49 There are several large Triassic-Jurassic terrestrial basins in West China, in which the Sichuan Basin has a relatively
50 complete and continuous continental sedimentary sequence of the Upper Triassic-Paleogene (e.g., SBGM, 1991, 1997;
51 Wang et al., 2010). During the Early Jurassic, the Sichuan Basin was in a Boreotropical climate zone based on
52 climate-sensitive sediments (Fig. 1a. Boucot et al., 2013), or a warm temperate climate is suggested based on clay mineralogy
53 and phytogeography (e.g., Dera et al., 2009). In this work, we present a field investigation, including lithofacies and paleosol

54 interpretation, and carbon and oxygen isotope analyses of both lacustrine and pedogenic carbonates in Sichuan Basin. New
55 results allow us to reconstruct the paleoclimate and relatively consecutive $p\text{CO}_2$ record through the Early Jurassic, for which
56 we compare to stable isotopes of marine sediments and estimated sea water temperature.

57 **2. Geological setting and stratigraphy**

58 Southwest China, including the provinces of Yunnan, Sichuan, Chongqing, and Guizhou, had been the main part of the
59 upper Yangtze Plate since the Proterozoic, possibly since the Neoproterozoic. With the amalgamation of the Cathaysia and
60 Yangtze plates, it became the western South China plate or cratonic basin since the Neoproterozoic (Sinian), and continued to
61 the late Middle Triassic. By the Indosinian orogeny, new foreland basins were formed since the Late Triassic (e.g., He and
62 Liao, 1985; Li et al., 2003), recording the Mesozoic and Cenozoic evolution of tectonics, environment, and climate in
63 Southwest China.

64 The Mesozoic Sichuan paleobasin was confined by the Longmenshan thrust belt in the northwest, the Micangshan-Dabashan
65 arcuate thrust belt in the northeast (Fig. 1b), and the northern hilly topography boundary of the Yunnan-Guizhou plateau in
66 the south and east. It was mainly developed during the Late Triassic-Jurassic and includes provincial areas of eastern
67 Sichuan, entire Chongqing, northern Guizhou, western Hubei, and northwestern Hunan. This Triassic-Jurassic Sichuan
68 foreland basin was much larger than the present Sichuan Basin in the eastern Sichuan province. We estimate the size of
69 Sichuan paleobasin is roughly 480,000 km² based on lithofacies paleogeography (Fig. 1b. Ma et al., 2009; Li and He, 2014),
70 and suggest naming this the grand Sichuan paleobasin (GSB).

71 The Mesozoic terrestrial sediments accumulated up to ~9 km (Guo et al., 1996) in the GSB; and the Jurassic part can be as
72 much as 3-3.5 km thick (SBGM, 1991). Two types of Lower Jurassic deposits have been distinguished (Table 1): the
73 Baitianba Formation (Fm) in the north (~10%) and the Ziliujing Fm (e.g., SBGM, 1991; Wang et al., 2010) in the south
74 (over 90% of the basin).

75 The Baitianba Fm was deposited unconformably on the Upper Triassic Xujiahe Fm and is overlain conformably by the
76 Middle Jurassic Xintiangou Fm / Qianfuyan Fm (Table 1). It is mainly composed of grayish shales and sandstones with coal
77 layers and massive conglomerates. Abundant plant fossils, sporopollens, conchostracans, bivalves, and gastropods indicate it
78 is of the Early Jurassic (SBGM, 1991, 1997). Sporopollen assemblages of the Hettangian-Sinemurian age were found in the
79 lower part (Zhang and Meng, 1987) and the Pliensbachian-Toarcian assemblages were reported in the upper part (Wang et
80 al., 2010).

81 The Ziliujing Fm is composed of variegated and reddish mudrocks (some shales) intercalated with sandstones, siltstones, and
82 bioclastic limestones as well as dolomitic marlstones / limy dolomites, conformably or unconformably overlying the Xujiahe
83 Fm or Luqiao Fm and conformably underlying the Xintiangou Fm (SBGM, 1997. Table 1). It has been dated as the Early

84 Jurassic by fossil assemblages of bivalves, ostracods, conchostracans, and plants. Dinosaur fauna can be well correlated to
85 the Lufeng Fauna in central Yunnan (e.g., Dong, 1984; SBGM, 1991, 1997; Peng, 2009). This formation is subdivided into
86 five parts in an ascending order: the Qijiang, Zhenzhuchong, Dongyuemiao, Ma'anshan, and Da'anzhai members (SBGM,
87 1997. Table 1). Of these, the former two are sometimes combined as the Zhenzhuchong Fm (e.g., SBGM, 1991; Wang et al.,
88 2010).

89 The Da'anzhai Member is characterized by dark gray to black shales and bioclastic limestones with a southward increase of
90 reddish mudrocks (SBGM, 1991, 1997; Wang et al., 2010), and is regarded the sediment in a grand Sichuan paleolake (e.g.,
91 Ma et al., 2009; Li and He, 2014). Ostracod assemblages indicate it is the late Early Jurassic (e.g., Wei, 1982; Wang et al.,
92 2010). A Re–Os isochron age of 180.3 ± 3.2 Ma associated with an organic carbon isotope excursion indicates that the lower
93 Da'anzhai Member corresponds to the T-OAE (Xu et al., 2017).

94 The Ma'anshan Member is comprised of violet-red mudrocks with a few greyish, greenish thin-bedded fine sandstones and
95 siltstones, in which floral fossils are common (Li and Meng, 2003). The Dongyuemiao Member consists of greenish and
96 reddish mudrocks and siltstones with greyish bioclastic limestone and marlstone, of which abundant bivalve and plant fossils
97 were reported from eastern Sichuan and Chongqing (Li and Meng, 2003; Meng et al., 2003; Wang et al., 2010). The
98 Zhenzhuchong Member is dominated by violet red mudrocks/shales intercalated with thin-bedded sandstones and / or
99 siltstones and numerous plant fossils of the Early Jurassic affinity (e.g., Duan and Chen, 1982; Ye et al., 1986). Taken
100 together, fossil associations suggest that the three members were deposited in the middle-late Early Jurassic. The age
101 limitation of the overlying Da'anzhai Member and the correlation to the Lufeng dinosaur fauna places these members in the
102 Sinemurian – Pliensbachian, and the Zhenzhuchong and Dongyuemiao Fms are suggested to be the Sinemurian (Table 1).

103 The Qijiang Member is composed of quartz arenite interbedded/intercalated with dark shales. Coal seams are often seen in
104 the middle of the Qijiang Member. This member mainly occurs in the central part of the GSB. It is likely the earliest Jurassic,
105 possibly Hettangian age, but plant fossils cannot precisely indicate the age (Wang et al., 2010).

106 **3. Materials and methods**

107 We have measured sections and made detailed observations and descriptions of sedimentary characteristics for lithofacies
108 analysis at six outcrop sections (Locations A1 to A4, A6 and A7, Fig. 1). Published descriptions for other sections
109 (Locations A5, A8, and A9, Fig. 1) are integrated into our observations. Details of microscopic examination of sedimentary
110 rocks and analysis of sedimentary facies underpinning the climate analysis are attached as the supplementary data Note S1.
111 Below we state climate-sensitive sediment observation, carbon and oxygen isotope analyses, and estimate of $p\text{CO}_2$.

112 **3.1. Observation of climate-sensitive sediments**

113 Climate-sensitive sediments are mainly dolomites, gypsum, and paleosols, which are used to analyze the climate in this work

114 (Table S1).

115 Dolomites and gypsum are relatively easy to recognize in both field and under microscope. We distinguish dolomites from
116 limestones following Tucker (2011) and Flügel (2004). As Flügel (2004) stated, field distinctions of limestone and dolomite
117 can also be made although detailed differentiation of carbonate rocks is best performed in the laboratory. In field, we
118 recognize gypsum by particular structures such as chicken-wire cage, gypsum pseudomorph, and cluster of (0.5-1 cm) pore.
119 There are multiple classifications of paleosols (e.g., Wright, 1992; Mack et al., 1993; Retallack, 2001b; Imbellone, 2011),
120 mostly based on the US Soil Taxonomy. We recognized paleosols in the field based on color, structures, horizonation, root
121 traces, and textures, and followed the general classification paleosols by Mack et al. (1993) and Retallack (2001b). In this
122 paper, paleosols are described following the procedures of the Soil Survey Manual and classified according to Soil Survey
123 Staff (1998).

124 Within the measured and observed sections, paleosol profiles were mainly identified from the two main locations/sections
125 A4 and A6 (Figs. S1 and S2, and Table S2). Horizonation, BK horizon thickness, boundaries, structures, trace fossils,
126 rootlets, carbonate accumulations (calcretes), etc. were recorded (Table S2). Paleosols interpreted in other cited sections (Fig.
127 1) rely on the description of lithology, structure, and calcrete in the original references. Based upon a modification of the
128 Retallack (1998) categorization of paleosol maturity, the relative paleosol development (maturity) was assigned.

129 **3.2. Analyses of carbon and oxygen isotopes**

130 Ten lacustrine carbonate samples were analysed for carbon and oxygen isotopes from the Da'anzhai Member at the Shaping
131 section, Ya'an (Location A4, Fig. S1 and Table S3). 26 pedogenic carbonate samples were analyzed for carbon and oxygen
132 isotopes from 32 paleosols of the Ziliujing Fm at the same section (Fig. S1 and Table S4). Two or three microdrilling
133 powder samples (columns 7 and 8 in Table S4) were taken from the same individual calcrete for stable isotope analysis, and
134 then a mean value for each calcrete sample was calculated (columns 9 and 10 in Table S4).

135 At the field scale, calcretes are ginger-like and sporadically spaced within the soil horizon. We observed no linear and planar
136 calcretes that would indicate precipitation at or below the water table. Before drilling, thin-sections were petrographically
137 studied using polarized light microscopy and cathodoluminescence imaging. Micritic calcite is predominant in both
138 lacustrine and pedogenic carbonate samples, with no evidence for carbonate detritus in calcretes (Fig. 2a and 2b). The
139 micritic calcites used for stable isotope analyses are chiefly null- to non-luminescent, with <10% light orange and brownish
140 luminescence, indicating genesis primarily in the vadose zone. While luminescent calcretes indicate a high possibility of
141 hydrological influence (e.g., Mintz, et al., 2016), we sampled to avoid this. Based on petrography and CL imaging together
142 with the field observations, the dense micritic zones sampled for the stable isotope composition should give pristine $\delta^{13}\text{C}$
143 values that can be used to estimate $p\text{CO}_2$.

144 Microsampling of lacustrine and pedogenic carbonates focused on only micrites, avoiding diagenetic spar from cracks, veins,

145 and vug spaces. Powder samples were obtained using a dental drill (aiguille diameter $\phi=1-2$ mm).
146 Isotopic analyses were conducted on 0.3 ~ 0.5 mg powder samples. Powder samples were dried in an oven at 60°C for 10
147 hours before being moved to the instrument. Carbon dioxide for isotopic analysis was released using orthophosphoric acid at
148 70°C and analysed on-line in a DELTA-Plus xp (CF-IRMS) mass spectrometer at the State Key Laboratory for Mineral
149 Deposits Research, Nanjing University. The precision of the measurements was regularly checked with a Chinese national
150 carbonate standard (GBW04405) and the international standard (NBS19) and the standard deviation of $\delta^{13}\text{C}$ was $\pm 0.1\%$ over
151 the period of analysis. Calibration to the international PeeDee Belemnite (PDB) scale was performed using NBS19 and
152 NBS18 standards.

153 3.3. Calculation of atmospheric CO₂ concentration

154 The Cerling (1991, 1999) equation was used to calculate the $p\text{CO}_2$ using the carbon isotope of pedogenic carbonates as
155 below:

$$156 \quad C_a = S_{(z)}(\delta^{13}\text{C}_s - 1.0044\delta^{13}\text{C}_r - 4.4)/(\delta^{13}\text{C}_a - \delta^{13}\text{C}_s)$$

157 where C_a is $p\text{CO}_2$; $\delta^{13}\text{C}_s$, $\delta^{13}\text{C}_r$, $\delta^{13}\text{C}_a$ are the isotopic compositions (‰) of soil CO₂, soil-respired CO₂, and atmospheric CO₂,
158 respectively; and $S_{(z)}$ is the CO₂ contributed by soil respiration (ppmV).

159 $\delta^{13}\text{C}_s$ is often calibrated by fractionation factor -8.98% with the formula $-8.98\% + \delta^{13}\text{C}_c$ (Ekart et al., 1999), with which $\delta^{13}\text{C}_c$
160 is the measured result of pedogenic calcrite. Alternatively, $\delta^{13}\text{C}_s$ can be replaced by $\delta^{13}\text{C}_{sc}$, which is calibrated by carbon
161 isotope ratio of pedogenic carbonate at 25°C based on latitude–temperature correlations (Besse and Courtillot, 1988; Ekart et
162 al., 1999) following the equation $\delta^{13}\text{C}_{sc} = (\delta^{13}\text{C}_c + 1000)/((11.98 - 0.12 * T)/1000 + 1) - 1000$ (Romanek et al., 1992). We used
163 both $\delta^{13}\text{C}_s$ and $\delta^{13}\text{C}_{sc}$ to calculate the $p\text{CO}_2$ (Table S4).

164 $\delta^{13}\text{C}_r$ represents carbon isotope ratio of average bulk C3 vascular tissue (Arens et al., 2000), reflecting atmospheric $\delta^{13}\text{C}$
165 (Jahren et al., 2008). The $\delta^{13}\text{C}_{om}$ of organic matter within paleosols based on the range of modern C3 ecosystem
166 fractionations (Buchmann, et al., 1998; Ekart et al., 1999), is commonly used for $\delta^{13}\text{C}_r$. However, the $\delta^{13}\text{C}_r$ could be
167 compromised in fossil soils due to oxidation and metabolism of organic matter after burial (Nadelhofer and Fry, 1988). In
168 this paper, we use the $\delta^{13}\text{C}_{om}$ from the Paris Basin (Bougeault et al., 2017; Peti et al., 2017) for the Sinemurian-Pliensbachian
169 $\delta^{13}\text{C}_r$ and from Cardigan Bay, UK (Xu et al., 2018) for the Toarcian.

170 $\delta^{13}\text{C}_a$, the carbon isotopic composition of the atmosphere, was about -8% in the 1980s, being depleted relative to the
171 pre-industrial atmosphere which was around -6.5% (Friedli et al., 1986). The average value of -6.5% has been chosen as the
172 $\delta^{13}\text{C}_a$ for acquiring $\delta^{13}\text{C}_r$ and $S_{(z)}$ (e.g., Ekart et al., 1999; Robinson et al., 2002), and the $\delta^{13}\text{C}_a$ was generally calibrated as
173 $\delta^{13}\text{C}_{ac}$ from $\delta^{13}\text{C}_r$ using the formula $(\delta^{13}\text{C}_r + 18.67)/1.1$ (Arens et al., 2000). Herein we used both calibrations to calculate the
174 $\delta^{13}\text{C}_a$ (Table S4).

175 $S_{(z)}$ is the largest source of uncertainty in $p\text{CO}_2$ estimates (Breecker, 2013) and the uncertainty arises primarily from their
176 sensitivity to soil-respired CO_2 ($S_{(z)}$) (Montañez, 2013). It is a function of depth and effectively constant below 50 cm (e.g.,
177 Cerling, 1991). $S_{(z)}=2500$ ppmV is suggested for the sub-humid temperate and tropical climates (Breecker et al., 2010),
178 2500-5000 ppmV for higher moisture and productivity soil (Montañez, 2013), 2000 ppmV for semi-arid areas (Breecker et
179 al., 2009), 1500-2000 ppmV for aridisols and alfisols (calcisol-argillisol) and 2000 ± 1000 for paleo-vertisol (Montañez,
180 2013), and 1000 ppmV in desert areas (Breecker et al., 2010) or 400 ± 200 ppmV for immature soil (Montañez, 2013). In
181 this context, we chose the $S_{(z)}=2000$ ppmV for calculating $p\text{CO}_2$ at 25°C as the calcisols are reddish-brownish aridisols, and
182 we also compared the results with that by $S_{(z)}=2500$ ppmV (Table S4). Additionally, we took samples at the middle and
183 lower Bk horizon (often $> \sim 20\text{-}30$ cm to the BK top). That means the depth of calcrete samples in the examined palaeosols
184 was generally deeper than 50 cm below the paleosol surface, meeting the requirement for a constant value of $S_{(z)}$.

185 **4. Results**

186 Based on the investigation of cross-sections (locations A1-A4, and A6-A7. Fig. 1), we have classified six sedimentary facies
187 units in the Ziliujing Fm. They are alluvial fan, fluvial river, flood plain, lake, lake-delta, and swamp facies. Details of
188 description and interpretation are in the supplementary data Note S1. Below are results of climate-sensitive sediment
189 observation, stable isotope analyses, and $p\text{CO}_2$ calculation.

190 **4.1. Climate-sensitive sediments**

191 Field observation combined with published calcrete materials shows that paleosols widely occur in the Lower Jurassic
192 Ziliujing Fm of the GSB (Figs. 1, 3, and 4). A total of 32 paleosols were observed and described at the Shaping section,
193 Ya'an, and five paleosols were found at the Tanba section, Hechuan (Table S2).

194 Most of paleosols are reddish (GSA Munsell Rock-Color 5R 2/2, 5R 3/4, 5R 4/2) and brownish (10R 3/4, 10R 5/4) (Fig. 3
195 and Table S2). Peds of paleosols are mainly angular and subangular, and a few are prismatic and platy. Slickensides are
196 common. Mottles (Fig. 3a), rootlets /rhizoliths (Fig. 3c), and burrows sometimes occur with strong leaching structures (Fig.
197 3a). Occasionally mudcracks are associated with the aforementioned structures (Fig. 3d).

198 All paleosols are calcic with more or less calcretes in Bk horizons. The thickness of Bk horizons mainly changes from 30 cm
199 and 100 cm, and partly up to 170 cm (Table S2). Calcretes are generally ginger-like, ellipsoid, subglobular, and irregular in
200 shape (Fig. 3b and 3e) and nodules are 1-3 cm even up to 8-15 cm (paleosols J1z-10-01 and J1z-12-01) in size (Fig. 3e).
201 Calcrete is often less than 0.5-1% in an individual paleosol, but a few can be up to 3-5% (paleosol J1z-3-01. Fig. 3b) even 10%
202 (paleosols J1z-5-02 and 18HC-10).

203 All above paleosols are defined as relatively mature calcisols (Mack et al., 1993), a kind of aridisol (Soil Survey Staff, 1998;
204 Retallack, 2001b). The original lithofacies were chiefly argillaceous and silty (split-fan) overbank, interchannel, and flood

205 plain deposits (Figs. S1 and S2). Some formed landward the paleo-lakeshore.
206 Dolomites were found at seven loactions in central and southern GSB (Figs. 1, 4, and Table S1). The dolomites chiefly occur
207 in the Toracian Da'anzhai Member and a few in the Sinemurian-Plienbachian Dongyuemiao and Ma'anshan members (Fig.
208 4). They are often massive whitish (Figs. 3f and S3e) and micritic (Figs. S4b and S4d), likely indicating an authigenic origin.
209 Gypsum is recorded in two loactions (Figs. 1, 4, and Table S1). One is located at Zigong (Location A5. SBG, 1980a). The
210 other lies at Hechuan (Location A6), which can be identified by chicken-wire cage structure and is associated with micriditic
211 dolomites (Fig. 3f).

212 4.2. Carbon and oxygen isotope values

213 $\delta^{13}\text{C}$ values of lacustrine carbonate samples range from -2.02‰ to -4.07‰ and $\delta^{18}\text{O}$ values range from -9.91‰ to -12.28‰
214 (Table S3 and Fig. 5). An increasing trend of both carbon and oxygen isotope ratios is observed from lower to upper
215 horizons across a 45 m stratal interval of the lower Da'anzhai Member (Fig. 6).

216 Pedogenic carbonate samples have $\delta^{13}\text{C}$ values from -3.52‰ to -8.10‰, which fall in the typical stable isotope range for
217 pedogenic carbonates. Values of -6‰ to -8.0‰ characterize the sequence of the Zhenzhuchong Member and main
218 Ma'anshan Member, with an abrupt increase to -5.5‰ to -3.5‰ at the top of Ma'anshan Member (samples J1z-16-01 and
219 J1z-18-01. Fig. 6). $\delta^{18}\text{O}$ values are mainly from -11.3‰ to -13.10‰ in the interval of the Zhenzhuchong Member and
220 Ma'anshan Member. $\delta^{18}\text{O}$ follows $\delta^{13}\text{C}$ with a sudden increase to -5.5‰ at the top of the Ma'anshan Member (Fig. 6). Large
221 and frequent variations of both carbon and oxygen isotope ratios can be observed in the lower Da'anzhai Member (Fig. 6 and
222 Table S4).

223 4.3. CO₂ concentrations

224 $p\text{CO}_2$ values based on paleobarometer modelling of paleosol calcite (Cerling, 1999) vary depending on the parameters used
225 for the calculation.

226 If $S_{(z)}=2500$ ppmV and $\delta^{13}\text{C}_a=-6.5$ ‰ (constant pre-industrial atmosphere), $p\text{CO}_2$ values range between ~1140 ppmV and
227 ~3460 ppmV with a mean of 1870 ppmV (column 15 in Table S4); and when $S_{(z)}=2500$ ppmV and $\delta^{13}\text{C}_a=(\delta^{13}\text{C}_r+18.67)/1.1$,
228 $p\text{CO}_2$ values change between ~1230 ppmV and ~3260 ppmV with a mean of 2070 ppmV (column 16 in Table S4).

229 When $S_{(z)}=2000$ ppmV and $\delta^{13}\text{C}_s=-8.98+\delta^{13}\text{C}_c$ are used, $p\text{CO}_2$ values are ~ 940-2530 ppmV with the mean 1600 ppmV
230 (column 17 in Table S4); and if $S_{(z)}=2000$ ppmV and $\delta^{13}\text{C}_s = (\delta^{13}\text{C}_c+1000) / ((11.98-0.12*25) / 1000+1) -1000$ are adopted,
231 $p\text{CO}_2$ values become ~980 ppmV to ~2610 ppmV with the mean 1660 ppmV (column 18 in Table S4). Details of the
232 different parameters and $p\text{CO}_2$ results can be seen in Table S4.

233 Results show that $p\text{CO}_2$ values at $S_{(z)}=2500$ ppmV are larger than at $S_{(z)}=2000$ ppmV and the $S(z)$ is largest uncertainty
234 leading to different $p\text{CO}_2$ values. The highest difference of $p\text{CO}_2$ is ~ 1000 (3463-2498) ppmV (Sample J1Z-18-01 at depth

182.6 m), while the lowest is ~245 (1226-981) ppmV (Sampe J1Z-12-01 at depth 148.9 m), and the mean is ~ 360 ppmV. In addition, when $S_{(z)}$ is the same, the $p\text{CO}_2$ values are close even if other parameters are different (comp. between columns 15 and 16, 17 and 18 in Table S4, and Fig. 6).

Whatever parameters used, the trend of $p\text{CO}_2$ over the epoch is quite similar (Fig. 6). We chose $S_{(z)}=2000$ ppmV (column 18 in Table S4) to illustrate the nature of the Early Jurassic $p\text{CO}_2$ in the GSB.

$p\text{CO}_2$ values mostly range between 980 ppmV and 2610 ppmV, and the mean 1660 ppmV is ~6 times the pre-industrial 275 ppmV. Most of the $p\text{CO}_2$ values are 1000-2000 ppmV with the mean 1580 ppmV in the Zhenzhuchong and Ma'anshan members, ~3.5-7.5 times the pre-industrial $p\text{CO}_2$ value.

It is noted that the errors of $p\text{CO}_2$ range from 384 ppmV to 1017 ppmV with a mean 647 ppmV (Table S5), leading to a large uncertainty of the mean ~39%. The largest source of the uncertainty is the standard error (766 ppmV) of modern soil carbonate (Breecker and Retallack, 2014). The $p\text{CO}_2$ uncertainty decreases by ~ 20% if half (383 ppmv) of the standard error of soil carbonate is selected, and decreases to ~12% if 1/4 (~191 ppmV) standard error is used. The second largest source of error in the $p\text{CO}_2$ is the $S_{(z)}$ estimate. The uncertainty of $p\text{CO}_2$ becomes much smaller when the $S_{(z)}$ is larger, e.g., it will fall from ~39% to ~17% if $S_{(z)}=5000$ ppmV instead of 2000 ppmV. Other parameters such as temperature, $\delta^{13}\text{C}_r$, $\delta^{13}\text{C}_a$, $\delta^{13}\text{C}_s$, contribute very little to the calculated $p\text{CO}_2$ uncertainty. The uncertainty of $p\text{CO}_2$ is same when either $\delta^{13}\text{C}_a$ is determined by the transfer from $\delta^{13}\text{C}_c$ of marine planktonic fossil carbonates (Table S8) or organic matters (Table S5).

251 **5. Discussion**

The Jurassic marine record shows climatic and environmental oscillations (e.g., van de Schootbrugge et al., 2005; Dera et al., 2011; Gómez et al., 2015; Arabas et al., 2017), including sea water temperature fluctuation and carbon cycle reorganization recorded in both carbonate and organic matter. The climate changes and events recorded in the the marine realm have been mainly attributed to Karoo-Ferrar volcanism (e.g., Hesselbo et al., 2000; Caruthers et a., 2013), sea-level change (e.g., Hesselbo and Jenkyns, 1998; Hallam and Wignall, 1999), orbital forcing (e.g., Kemp et al., 2005; Huang and Hesselbo, 2014, Storm et al., 2020), and / or the opening of the Hispanic corridor (e.g., van de Schootbrugge et al., 2005; Arias, 2009). Eruption of the Karoo-Ferrar and Central Atlantic mgama is thought to have released large amounts of CO_2 into the atmosphere in a short amount of time, resulting in rising temperatures of both marine and continental realms. The nearly continuous record of Jurassic strata in the GSB provides an excellent test of this hypothesis in the terrestrial realm. We compare the climate and $p\text{CO}_2$ record from the GSB in relationship to the marine temperature records.

262 **5.1. Paleoclimate variation**

263 During the Late Triassic, Southwest China was warm-hot and humid and occupied a tropical and / or subtropical zone, as
264 demonstred by palynoflora, coals, and perennial riverine and lacustrine lithofacies in the Xujiahe Fm (e.g., Huang, 1995; Li

265 et al., 2016). However, the climate became dry through the Early Jurassic manifested by climate-sensitive sediments and
266 stable isotopes albeit there are two lithofacies packages reflecting two major lake stages (for details refer to supplementary
267 data Note S1) in the GSB.

268 **5.1.1 The Hettangian Age**

269 In the Hettangian, the climate was warm-humid like the Late Triassic in the GSB. The Qijiang Member is comprised of
270 mainly mature quartz arenites and siltstones with coals (Fig. 7) as well as siderite concretions, indicating a stable tectonic
271 setting and warm-humid climate in the eastern and southern GSB. Climate was similar across the whole region, because
272 multiple coal layers occur in the lower Baitianba Fm. The alluvial fan system of the lower Baitianba Fm. (Figs. 7 and S6) is
273 characterized by moderate-good roundness and sorting of gravels with sandy matrix (Fig. S3a. e.g., Liu et al., 2016; Qian et
274 al., 2016; and this work). In the Newark basin of eastern North America, climate-sensitive sediments such as nodules of
275 carbonate and gypsum (pseudomorph) as well as mudcrack in mudflat facies indicate an arid climate in the fifth cycle of the
276 Hettangian (>199 Ma) Passaic Fm (Kent et al., 2017). More widespread, the eolian Navajo Sandstone, dated as
277 Hettangian-Sinemurian (200-195 Ma. Parrish et al., 2019), indicates arid in Colorado Plateau (Fig. 1a. Boucot et al., 2013).

278 **5.1.2 The Sinemurian Age**

279 The early Sinemurian Zhenzhuchong Member is a combination of riverine flood plain and lacustrine facies (supplementary
280 Note S1). The lithology is dominated by violet-red mudrocks with few thin greyish, greenish fine sandstones and siltstones.
281 The reddish color of rocks may indicate a change of climate. Differences in the color appearance show that the reddish color
282 started in the middle member in the central basin (Location A6. Fig. S2) but almost developed through the whole member in
283 the western basin (Location A4. Fig. 6).

284 Within reddish mudrocks of the flood plain facies, multiple calcisols were observed at the Shaping section, Ya'an (Location
285 A4. Figs. 1, 4, and 7), including a strongly leached calcisol horizon (Fig. S3c). We also interpret the reddish muddy
286 sediments with abundant calcretes as the calcisol at sections of Dafang (Location A8. Zhang et al., 2016), Tianzhu (Location
287 A9. Li and Chen, 2010), and Weiyuan (Location A10. SBG, 1980a). The calcisols indicate a (semi-) arid climate in the
288 Sinemurian.

289 This climate change, interpreted from reddish mudrocks and paleosols, is consistent with the floral fossils (e.g., Huang, 2001;
290 Wang et al., 2010), suggesting the decreasing humidity and increasing temperature from the Late Triassic epoch and the
291 Hettangian age into the Sinemurian age in the southern GSB. However, in the northern GSB there are few proxies for
292 climate change, and alluvial fan and lacustrine delta facies common in the middle Baitianba Fm (Fig. S6. e.g., Qian et al.,
293 2016) do not give us information on climate.

294 The late Sinemurian Dongyuemiao Member also has reddish mudrocks and calcisols, similar to the Zhenzhuchong Member.

295 Pedogenic calcretes were reported at Dafang (Location A8. Zhang et al., 2016), Tianzhu (Location A9. Li and Chen, 2010),
296 and Yunyang (Location A15. Meng et al., 2005) and in the central and southern GSB (Figs 4 and 7 and Table S2), indicating
297 continued arid climate conditions at the time.

298 The interpreted Sinemurian (semi-) arid climate from reddish mudrocks and calcisols is supported by the flora (Li and Meng,
299 2003) and the mudrock geochemistry (Guo et al., 2017). Few records of coeval terrestrial climate are known from other
300 continents or regions in the literature. The Whitmore Point Member of the Moenave Fm deposited in dryland lakes (Tanner
301 and Lucas, 2008) and the upper part of eolian Navajo Sandstone (Blakey et al., 1988) could represent the coevally similar
302 climate in Colorado Plateau although relatively cool (~9 to 18 °C) continental climate was inferred from oxygen and
303 hydrogen isotope composition of chert precipitated in interdune, freshwater lakes in the Navajo Sandstone (Kenny, 2015).
304 With a difference, in eastern England, the co-occurrence of the acmes of thermophilic pollens *Classopollis classoides* and
305 *Liasidium variable* indicates the warm-humid climate in the late Sinemurian (Riding et al., 2013).

306 **5.1.3 The Pliensbachian Age**

307 The Ma'anshan Member of the Pliensbachian displays a prominent change in the distribution and extent of red color
308 sediment and pedogenesis. The reddish sediments extend through the entire member (comp. Figs. 6 and S2) and can be
309 observed across most of the GSB. Calcisols are documented in both the western and central GSB (Figs. 6, 7, S1, and S2).
310 Ten calcisol horizons were recognized at the Shaping section, Ya'an (Figs. 6 and S1). Strongly leached pedogenic structures
311 and mudcracks are seen in Bed H8 of the Tanba section, Hechuan (Fig. 3a and 3d). Abundant calcretes within terrestrial red
312 mudrocks are widely described at Gaoxian of Dafang (Location A8. Zhang et al., 2016), Hulukou of Weiyuan (Location A10.
313 SBG, 1980a), Geyaoguan of Gulin (Location A13. SBG, 1976), Taiyuan of Fengdu (Location A16. SBG, 1975), and Yaxi of
314 Zunyi (Location A17. Yang, 2015). The widespread distribution of redbeds and calcisols (Figs. 4 and 7) denotes an
315 intensification of the (semi-) arid climate.

316 Plant and sporopollen fossils also show a change to drier climate in the Pliensbachian. Compared to the Sinemurian members,
317 more plant fossils are reported in this member (e.g., Meng and Chen, 1997; Wang et al, 2010). The Pliensbachian-Toarcian
318 sporopollen assemblages are dominated by sporomorph genera assemblage *Dictyophyllidites-Cyathidites-Classopollis*, in
319 which the dry-type gymnosperm spore *Classopollis* is more prevalent than in the Hettangian-Sinemurian (Zhang and Meng,
320 1987).

321 Similar dry temperate / subtropical climate is interpreted for the upland coniferous forest in Qaidam Basin, Northwest China
322 (Wang et al., 2005) and by interdune playa mudstones of the Kayenta Fm in Colorado Plateau (e.g., Bromley, 1992) albeit it
323 was a cool-humid climate in South Kazakhstan, central Asia (Tramoy et al., 2016).

324 5.1.4 The Toarcian Age

325 In spite the fact that the Da'anzhai Member was deposited in the largest lacustrine transgression period (Fig. 7. details see
326 supplementary data Note S1), abundant evidence for arid conditions, including backshore reddish mudrocks with calcisols,
327 lacustrine micritic dolomites and / or gypsum, and stable isotopic geochemistry of lacustrine carbonate, indicate that the
328 Toarcian aridification could be the most intensive of the late Early Jurassic in the GSB.

329 Redbeds with abundant calcretes are well developed in this member (Figs. 4 and 7). Four calcisols in the Shaping section
330 (Figs. 6 and S1) and the leaching/illuvial structure (Bed H13) in the Tanba section (Fig. 3c) were observed. Calcisols with
331 calcretes also occur at sections of Dafang (Location A8. Zhang et al., 2016), Nanxi (Location A11. SBG 1980a), Gongxian
332 (Location A12. Liang et al., 2006), and Yunyang (Location A15. Meng et al., 2005). The widespread occurrence of calcisols
333 within the lacustrine facies reveals that subaerial exposure of sediments often interrupted the lake environment, illustrating
334 dynamic lake level fluctuations and an arid climate.

335 Gypsum and micritic dolomites are reported in the western and southern GSB (SBG, 1980a; Mo and Yu, 1987; Peng, 2009;
336 and this work) (Figs. 1, 4, and 7). Though there are a number of hypotheses on the dolomite formation in deep time, such as
337 authigenic origin, diagenetic replacement, microbial mediation (e.g., Vasconcelos et al., 1995; Mckenzie et al., 2009; Petrash
338 et al., 2017), a high abundance of dolomite was interpreted to form during greenhouse periods, characterized by warm
339 climates, probably reflecting favourable conditions for evaporite deposition and dolomitization via hypersaline reflux
340 (Warren, 2000). Dolomites are also thought the results of interplay of climate and sea-level / base-level change (e.g.,
341 Newport et al., 2017) or are interacted with climatic regimes (Vandeginste et al., 2012). The widespread micritic dolomites
342 in the Da'anzhai Member, which are associated with gypsum (Fig. 3f), likely indicate an arid climate in the central and
343 western GSB (Fig. 1b). Gypsum occasionally occurs at Maliuping of Hechuan (Fig. 3f) and Wujiaba of Zigong (SBG,
344 1980a), showing a possible evaporitic climate in the early Toarcian in the central GSB.

345 Carbon and oxygen isotopes of lacustrine carbonates further support the interpretation of an arid climate in the Toarcian age
346 in the GSB. The mainly positive $\delta^{13}\text{C}$ values 0 to 2 ‰ (Fig. 5) from Hechuan (Wang et al., 2006) indicate the lakes were
347 brackish or even saline. The relatively heavy negative $\delta^{13}\text{C}$ values -1‰ to -3.5 ‰ (Fig. 5) from Zigong (Wang et al. 2006)
348 and Ya'an (this work) denote low depletions of ^{13}C during calcite/aragonite precipitation and mean that the lakes were
349 possibly brackish. Lightly negative $\delta^{18}\text{O}$ values -5‰ to -12 ‰ (Fig. 5) of the lacustrine carbonates, suggest closed lacustrine,
350 palustrine and pond systems formed in a regional arid-semiarid climate with evaporation exceeding precipitation.

351 The covariance of $\delta^{13}\text{C}$ and $\delta^{18}\text{O}$ is a criterion to distinguish closed or open lakes (e.g., Talbot, 1990; Li and Ku, 1997).
352 Pronounced positive covariances ($R^2=0.44-0.96$) between carbon and oxygen isotopes (Fig. 5) indicate a typical
353 arid-semiarid pattern of lakes in the central and western GSB.

354 The Da'anzhai Member has the same palynofloral assemblage with the Ma'anshan Member, in which the dry-type

355 gymnosperm spore *Classopollis* is more abundant than in underlying strata (e.g., Zhang and Meng, 1987; Wang et al., 2010),
356 supporting the aridification indicated by climate-sensitive sediments and stable isotope ratios of lacustrine carbonates
357 aforementioned.

358 Coastal Cheirolepidiacean (gymnosperm) forests indicate (temperate to subtropical) warm-humid climate punctuated by
359 locally dry and/or arid events in the Toarcian in Qaidam Basin, Northwest China (Wang et al., 2005). In Inner Mongolia of
360 North China, the thermophilous plants such as the dipteridaceous fern *Hausmannia*, bennettitales *Ptilophyllum*, display
361 similar warm and humid climate interrupted by hot and even arid conditions in a short intervals of the Toarcian (Deng et al.,
362 2017). The warm-wet climate was also indicated by assemblages of sporomorph and vegetation in the late Early Jurassic in
363 Jurong of Jiangsu, Lower Yangtze area (Huang et al., 2000). In South Kazakhstan, central Asia, paleoflora and $\delta^2\text{H}$ values
364 suggest slightly less humid and warmer conditions starting from the early Toarcian (Tramoy et al., 2016).

365 Climate-sensitive sediments, carbon and oxygen isotope values and covariance, and palynoflora, together indicate that an
366 overall (semi-) arid climate dominated the GSB during the Early Jurassic, possibly accompanied by occasional evaporitic
367 climate. Relatively abundant calcisols suggest that the GSB was in a subtropical arid zone based on the paleoclimatic
368 zonation model of paleosols (Mack and James, 1994) during the middle-late Early Jurassic. Through the Early Jurassic, this
369 (semi-) arid climate in GSB is thoroughly comparable with the simultaneous arid climate recorded in dryland lacustrine and
370 eolian facies in Colorado Plateau (e.g., Blakey et al., 1988; Bromley, 1992; Tanner and Lucas, 2008; Parrish et al., 2017), but
371 distinct from the relatively warm-humid climate indicated by sedimentological and floral characteristics in North China (e.g.,
372 Wang et al., 2005, Deng et al., 2017) and in the relatively high latitudes of Southern Hemisphere (Pole, 2009).

373 In summary, the increasing aridity and warming in the GSB and arid climate in the Colorado Plateau could have been
374 consecutive through the Early Jurassic, and seems not harmonized with the global fluctuated climate that could be
375 imprinted by two large volcanic eruptions of the Central Atlantic magmatic province and Karro-Ferrar Large Igneous
376 Province. The secular arid climate in the two areas might be more possibly constrained by paleotopography, where both were
377 laid in the relatively low latitudes 15-30°N (Fig. 1a).

378 **5.2. $p\text{CO}_2$ perturbations and events**

379 Pedogenic carbonates found in various continental settings precipitate in direct contact with soil atmosphere and bed rock
380 and hold a meaningful signature of past climate (Alonso-Zarza and Tanner, 2006). There are few high age resolution $p\text{CO}_2$
381 reconstructions for the Early Jurassic. The focus on $p\text{CO}_2$ estimates has on the event horizons, such as the transition of the
382 Triassic to Jurassic (e.g., Tanner et al., 2001; Schaller et al., 2011). Herein we present a $p\text{CO}_2$ estimate based on data from
383 the GSB at ~ 1.0 Myr age resolution for ~ 20 Myr (199-179 Ma) interval of the Early Jurassic (Figs. 6 and 8a).

384 5.2.1. $p\text{CO}_2$ perturbation

385 Results of model estimates show that the $p\text{CO}_2$ values range 980-2610 ppmV with a mean 1660 ppmV in the Early Jurassic
386 post the Hettangian and can be divided into three intervals (Figs. 6 and 8a): phase I, stable 1500-2000 (mean ~1700) ppmV
387 in the Zhenzhuchong and Dongyuemiao members (Sinemurian age); phase II, main 1000-1500 (mean ~ 1300) ppmV in the
388 Ma'anshan Member (Pliensbachian age); and phase III, great fluctuation 1094-2610 (mean ~1980) ppmV in the lower
389 Da'anzhai Member (early Toarcian age).

390 The evolution and level of $p\text{CO}_2$ estimated by carbon isotope ratios of the pedogenic carbonates from the GSB compare
391 favorably with the global composite based on the plant stomata method (data of the composite curve see Table S6), but show
392 significant differences relative to the global composite $p\text{CO}_2$ based on paleosols (Fig. 8a. Suchecki et al., 1988; Cerling,
393 1991; Ekart et al., 1999), which may be attributed to the shortage (<4 samples) of global data and large age uncertainties (Fig.
394 8a and Table S5 and S6).

395 The changes in $p\text{CO}_2$ from the GSB, has a similar pattern to coeval seawater temperature estimates through the Early
396 Jurassic although there are some discrepancies in pace and in detail (comp. Fig. 8a and 8b). That is, the relatively high $p\text{CO}_2$
397 1500-2000 ppmV approximately corresponds to the relatively high seawater mean temperature -2°C to $+2^\circ\text{C}$ in the
398 Sinemurian, low $p\text{CO}_2$ 1000-1500 ppmV corresponds to low seawater mean temperature -5°C to -2°C in the Pliensbachian,
399 and quick rising $p\text{CO}_2$ of 1200 ppmV to ~2500 ppmV corresponds to the rapidly increased seawater temperature of -4°C to
400 $+4^\circ\text{C}$ in the late Pliensbachian-early Toarcian.

401 The $p\text{CO}_2$ record roughly trends with the carbon isotope records of marine carbonates and organic matter (comp. Fig. 8a to
402 8d), suggesting a possible linkage of the $p\text{CO}_2$ record in the GSB to the global carbon cycle (see section 5.2.2). Nevertheless,
403 it is difficult for the proxies to compare in a higher detail, making it difficult to relate the record to orbital forcing of the
404 global carbon cycle in the Sinemurian-Pliensbachian (Storm et al., 2020).

405 As a greenhouse gas, atmospheric CO_2 has a strong control over global temperatures for much of the Phanerozoic (e.g.,
406 Crowley and Berner, 2001; Royer, 2006; Price et al., 2013), but a decoupling of CO_2 and temperature has also been
407 suggested (e.g., Veizer et al., 2000; Dera et al., 2011; Schaller et al., 2011). The pattern of the Early Jurassic $p\text{CO}_2$
408 reconstructed from the carbon isotope of pedogenic carbonates in GSB, Southwest China, supports the coupled relationship
409 of CO_2 -temperature. Models of the coupling and decoupling of CO_2 -temperature and CO_2 -carbon cycle have to consider: 1),
410 age order of CO_2 -temperature/carbon cycle relevance, i.e. they should be related in the same age (long term or short term)
411 hierarchy; 2) precise age constraints of individual CO_2 and temperature data; 3) methods of CO_2 and temperature estimates,
412 depending on precondition, presumptions, parameters, uncertainty, sample diagenesis, etc.; 4) controls or influences of key
413 factors such ice sheet, tectonic, paleogeography, cosmic ray flux, biota, volcanic eruption, and so on.

414 5.2.2. Rapid $p\text{CO}_2$ falling events

415 The GSB Early Jurassic $p\text{CO}_2$ curve reveals two rapid falling events (Fig. 6 and 8a). The first event ($1E_{\text{CO}_2}$) shows a quick
416 drop from ~ 2370 ppmV (sample J1z-08-01 at depth 84.7 m) to 1350 ppmV (sample J1z-10-02 at depth 94.4 m) near the
417 boundary of the Dongyuemiao and Ma'anshan Members (Fig. 6), or to 1075 ppmV (sample J1z-11-02 at depth 111.7 m),
418 which took place in the early Pliensbachian (~ 190.4 - $189.9/189.1$ Ma. Fig. 8c). The extent of the rapid falling $p\text{CO}_2$ is
419 ~ 1000 - 1300 ppmV in 9.7-17.0 m. In other words, ~ 1000 ppmV drop could be accomplished within ~ 0.5 - 1.0 Myr based on
420 the estimate of sedimentation rate (Table S4).

421 While the corresponding early Pliensbachian climatic and isotopic-shifting events are not observed in the smoothed curves of
422 the Early Jurassic seawater temperature and carbon cycle (Dera et al. 2011), the rapid falling event $1E_{\text{CO}_2}$ is well correlated
423 to the nearly coeval excursion events of carbon and oxygen isotopes recorded in western Tethys and North Atlantic (Fig. 8).
424 The $1E_{\text{CO}_2}$ compares well to: 1) the rapid carbon isotope negative excursion of (oysters, belemnites, and brachiopods) shells
425 from the Cleveland Basin, UK (Korte and Hesselbo, 2011) and northwest Algeria (Baghli et al., 2020), 2) that of organic
426 matter and marine carbonates from southern Pairs Basin (Bougeault et al., 2017; Peti, et al., 2017) and Cardigan Bay Basin,
427 UK (Storm et al., 2020), and 3) rapid oxygen isotope negative excursion (seawater warming) of belemnites from northern
428 Spain (van de Schootbrugge et al., 2005). The rapid change of the stable isotope record had been called the
429 Sinemurian-Pliensbachian boundary event (SPBE) and dated in the ammonite of the upper *Raricostatum* - lower *Jamesoni*
430 zones (Bougeault et al., 2017).

431 The second event $2E_{\text{CO}_2}$ displays a large drop of 2574 ppmV (sample J1z-18-01 at depth 252.7 m) to 1094 ppmV (sample
432 J1z-19-01 at depth 272.3 m), ~ 1500 ppmV decrease within 19.6 m (estimated age interval ~ 0.8 Myr. Table S4 and Fig. 8a).
433 Following the second drop, $p\text{CO}_2$ rises rapidly by ~ 1300 ppmV of 1094 ppmV to 2386 ppmV (sample J1z-20-01 at depth
434 294.3 m) although only a few samples support the this cycle of $p\text{CO}_2$ falling-rising.

435 Strata in western Sichuan (Xu et al., 2017), may correlate to the time interval of the T-OAE, during which $p\text{CO}_2$ doubled
436 over background values, from ~ 1000 ppmV to ~ 2000 ppmV (e.g., Beerling and Royer, 2002; McElwain et al., 2005; Berner,
437 2006). Given that chronostratigraphical correlation is challenging, the $p\text{CO}_2$ falling-rising cycle might correspond to the
438 quick shifting cycle of stable isotopes during the T-OAE (Fig. 8a and 8c-8d). In detail, the rapid falling-rising of $p\text{CO}_2$ is
439 consistent with: 1) the quick negative-positive carbon isotope excursion of marine carbonates from Italy (Jenkyns and
440 Clayton, 1986; Sabatino et al., 2009), England and Wales (Jenkyns and Clayton, 1997), north Spain (van de Schootbrugge et
441 al., 2005), the Lusitanian Basin of Portugal (Hesselbo et al., 2007), Paris Basin (Hermoso et al., 2009), and Morocco (Bodin
442 et al., 2016); 2) that of invertebrate calcareous shells from the Cleveland Basin of UK (Korte and Hesselbo, 2011) and
443 northwest Algeria (Baghli et al., 2020); 3) that of marine organic matter from Morocco (Bodin et al., 2016), Yorkshire of
444 England (Cohen et al., 2004; Kemp et al, 2005), Cardigan Bay Basin of UK (Xu et al., 2018), northern Germany (van de

445 Schootbrugge et al., 2013), Alberta and British Columbia of Canada (Them II et al., 2017), northern Tibet of China (Fu et al.,
446 2016), and Japan (Izumi et al., 2018); 4) that of terrestrial organic matter from Sichuan Basin, China (Xu et al., 2017); and 5)
447 quick oxygen isotope negative-positive shifting (seawater warming) of brachiopods (Suan et al., 2008) and fossil wood
448 (Hesselbo et al., 2007) from the Lusitanian Basin, Portugal.

449 Multiple hypotheses have been proposed to interpret the 5°–6 °C decrease of sea surface temperatures in the late
450 Pliensbachian (Bailey et al., 2003; van de Schootbrugge et al., 2005; Suan et al., 2010) and warming ~8 °C in the early
451 Toarcian (Bailey et al., 2003; Suan et al., 2010), such as the sea level falling and rising, methane release, Karoo–Ferrar
452 eruption, Hispanic corridor opening, etc. Perhaps, these hypotheses somewhat explain the rapid change of sea surface
453 temperatures, but might not link to drastic falling of $p\text{CO}_2$. As we know, atmospheric CO_2 is controlled by volcanism,
454 weathering, vegetation on land and phytoplankton in ocean, and orbiting forcing. The Sr isotope curve shows a rapid change
455 in the early Toarcian but does not in the early Pliensbachian (e.g., Jones et al., 1999), indicating a distinct transfer of
456 weathering took place on the land only at the T-OAE time. No robust evidence shows the rapid changes of terrestrial
457 vegetation and marine primary productivity for the two intervals except for the floral change in western Tethys during the
458 T-OAE (Slater et al. 2019). The Karoo–Ferrar eruption could be responsible for the rapid rising of $p\text{CO}_2$ but not for the
459 falling. Then the orbital forcing might be an alternative.

460 To sum up, the rapid falling events of the Early Jurassic $p\text{CO}_2$ values in the GSB, are compatible with the response of stable
461 isotopes (carbon cycle) and seawater temperature from coeval marine sediments in a total tendency and eventful change, but
462 not harmonized at a high-resolution time scale. Whatever caused the rapid variations of sea surface temperatures, stable
463 isotopes, and $p\text{CO}_2$, their near concordance suggests that it is a positive feedback of the sea surface temperature and carbon
464 cycle to the $p\text{CO}_2$ in trend and event through the Early Jurassic; whereas the higher frequency changes in the
465 Sinemurian-Pliensbachian might support other causal driving of the climate, such as orbital forcing (Storm et al., 2020).

466 **6. Conclusions**

467 Based on analyses of climate-sensitive sediments and stable isotopes and the reconstruction of paleoclimate and $p\text{CO}_2$, we
468 conclude:

- 469 1) An overall warm-hot and (semi-) arid climate dominated the GSB during the Early Jurassic, possibly accompanied by
470 occasional evaporitic climate in the Toarcian. This (semi-) arid climate in GSB is comparable with that in Colorado Plateau,
471 western America, but distinct from the relatively warm-humid terrestrial climate recognized in other places of Chinese
472 mainland (e.g., Qaidam, Inner Mongolia, and Lower Yangtze) and the high latitudes of Southern Hemisphere.
- 473 2) The Early Jurassic $p\text{CO}_2$ values show that a range between 980 ppmV and 2610 ppmV is ~3.5-10 times the pre-industrial
474 value 275 ppmV and the mean 1720 ppmV is ~6 times the pre-industrial value. Three phases of $p\text{CO}_2$ values were

475 distinguished: 1500-2000 (mean ~1700) ppmV in the Sinemurian age, 1000-1500 (mean ~ 1300) ppmV in the Pliensbachian
476 age, and 1094-2610 (mean ~1980) ppmV in the early Toarcian. Two events of rapidly falling $p\text{CO}_2$ were also recognized:
477 ~1000-1300 ppmV drop at the Sinemurian-Pliensbachian boundary and quick falling (-rising) by ~1500 ppmV in the early
478 Toarcian. The phases and events manifest the perturbation of $p\text{CO}_2$ in the Early Jurassic.

479 3) The perturbation and rapid falling events of the Early Jurassic $p\text{CO}_2$ from the GSB are compatible with the carbon cycle
480 and seawater temperature from coeval marine sediments in the North Atlantic and western Tethys in a total tendency and
481 eventful change. The compatibility suggests that it is a positive linkage of the sea surface temperature and carbon cycle to
482 the $p\text{CO}_2$ through the Early Jurassic. On the contrary, differences at a high-resolution time scale implies additional climate
483 drivers, such as orbital forcing are important in the Sinemurian-Pliensbachian record.

484 **Acknowledgements**

485 We thank Professors Helmut Weissert and Dan Breecker for careful scrutiny, constructive comments and suggestions. It is
486 acknowledged this research was supported by Natural Science Foundation of China (NSFC) project 41672097.

488 **References**

- 489 Alonso-Zarza, A. M. and Tanner, L. H.: Preface. *Geol. Soc. Am. Spe. Pap.*, 416, v-vii, doi, 10.1130/0-8137-2416-3.v, 2006.
- 490 Arabas, A., Schlogl, J., and Meiste C.: Early Jurassic carbon and oxygen isotope records and seawater temperature variations:
491 Insights from marine carbonate and belemnite rostra (Pieniny Klippen Belt, Carpathians), *Palaeogeogr. Palaeoclimatol.*
492 *Palaeoecol.*, 485, 119–135, 2017
- 493 Arens, N. C., Jahren, A. H., and Amundson, R.: Can C_3 plants faithfully record the carbon isotopic composition of
494 atmospheric carbon dioxide, *Paleobiology*, 26, 137–164, 2000,
- 495 Arias, C.: Extinction pattern of marine Ostracoda across the Pliensbachian-Toarcian boundary in the Cordillera Ibérica, NE
496 Spain: Causes and consequences, *Geobios*, 42, 1-15, 2009.
- 497 Baghli, H., Mattioli, E., Spangenberg, J. E., Bensalah, M., Arnaud-Godet, F., Pittet, B., and Suan, G.: Early Jurassic climatic
498 trends in the south-Tethyan margin. *Gondwana. Res.*, 77, 67-81, doi, 10.1016/j.gr.2019.06.016, 2020.
- 499 Bailey, T. R., Rosenthal, Y., McArthur, J. M., van de Schootbrugge, B., and Thirlwall, M. F.: Paleooceanographic changes of
500 the Late Pliensbachian-Early Toarcian interval: a possible link to the genesis of an Oceanic Anoxic Event, *Earth Planet.*
501 *Sci. Lett.*, 212, 307-320, 2003.
- 502 Beerling, D. J. and Royer, D. L.: Reading a CO_2 signal from fossil stomata, *The New Phytologist*, 153, 387-397, doi:0.
503 1046/j. 0028-646X. 2001. 00335. x, 2002.

504 Berner, R. A.: GEOCARBSULF: A combined model for Phanerozoic atmospheric O₂ and CO₂, *Geochi. Cosmochi. Ac.*,
505 70(23 Spec. Iss.), 5653-5664, 2006.

506 Besse, J., and Courtillot, V.: Paleogeographic maps of the continents bordering the Indian Ocean since the Early Jurassic: *J.*
507 *Geophys. Res.*, 93, 11791–808, 1988.

508 Blakey, R. C., Peterson, F., and Kocurek, G.: Synthesis of late Paleozoic and Mesozoic eolian deposits of the Western
509 Interior of the United States, *Sediment. Geol.*, 56, 3-125, doi, [https://doi.org/10.1016/0037-0738\(88\)90050-4](https://doi.org/10.1016/0037-0738(88)90050-4), 1988.

510 Bodin, S., Krencker, F. N., Kothe, T., Hoffmann, R., Mattioli, E., Heimhofer, U., and Kabiri, L.: Perturbation of the carbon
511 cycle during the late Pliensbachian – early Toarcian: New insight from high-resolution carbon isotope records in
512 Morocco, *J Afri. Earth Sci.*, 116, 89–104, doi, 10.1016/j.jafrearsci.2015.12.018, 2016.

513 Boucot, A. J., Chen, X., Scotese, C. R., and Morley, R. J.: *Phanerozoic Paleoclimate: An Atlas of Lithologic Indicators of*
514 *Climate*, SEPM Concepts in Sedimentology and Paleontology 11. SEPM, Tulsa, 1-478, 2013.

515 Bougeault, C., Pellenard, P., Deconninck, J. F., Hesselbo, S. P., Dommergues, J. L., Bruenau, L., Cocquerez, T., Laffont, R.,
516 Huret, E., and Thibault, N.: Climatic and palaeoceanographic changes during the Pliensbachian (Early Jurassic) inferred
517 from clay mineralogy and stable isotope (C-O) geochemistry (NW Europe), *Global Planet. Change*, 149, 139-152,
518 2017.

519 Breecker, D. O. and Retallack, G. J.: Refining the pedogenic carbonate atmospheric CO₂ proxy and application to Miocene
520 CO₂, *Palaeogeogr. Palaeoclimatol. Palaeoecol.*, 406, 1-8, 2014.

521 Breecker, D. O., Sharp, Z. D., and McFadden, L. D.: Atmospheric CO₂ concentrations during ancient greenhouse climates
522 were similar to those predicted for A. D. 2100, *PNAS*, 107, 2, 576-580, 2009.

523 Breecker, D. O., Sharp, Z. D., and McFadden, L. D.: Seasonal bias in the formation and stable isotope composition of
524 pedogenic carbonate in modern soil from central New Mexico, USA, *Geol. Soc. Am. Bull.*, 12, 630-640, 2010.

525 Breecker, D. O.: Quantifying and understanding the uncertainty of atmospheric CO₂ concentrations determined from calcic
526 paleosols. *Geochem. Geophys. Geosyst.*, 14, 3210–3220, 2013.

527 Bromley, M.: Topographic inversion of early interdune deposits, Navajo Sandstone (Lower Jurassic), Colorado Plateau,
528 USA, *Sediment. Geol.*, 80, 1-25, 1992.

529 Buchmann, N., Brooks, R. J., Flanagan, L. B., and Ehleringer, J. R.: Carbon isotope discrimination of terrestrial ecosystems.
530 In Griffiths, H., ed. *Stable Isotopes: Integration of Biological, Ecological and Geochemical Processes*, BIOS Scientific
531 Publications, Oxford, United Kingdom, 203–21, 1998.

532 Caruthers, A. H., Smith, P. L., Gröcke, D. R.: The Pliensbachian-Toarcian (Early Jurassic) extinction, a global multi-phased
533 event, *Palaeogeogr. Palaeoclimatol. Palaeoecol.*, 386, 104-118, 2013.

534 Cerling, T. E.: Carbon dioxide in the atmosphere: evidence from Cenozoic and Mesozoic paleosols: *Am. J. Sci.*, 291,
535 377-400, 1991.

536 Cerling, T. E.: Stable carbon isotopes in palaeosol carbonates, in: Palaeoweathering, palaeosurfaces and related continental
537 deposits, edited by: Thiry, M. and Simm-Coinçon, R., Spec. P Intl. Asso. Sedi., 27, 43-60, 1999.

538 Cleveland, D. M., Nordt, L. C., Dworkin, S. I., and Atchley, S. C.: Pedogenic carbonate isotopes as evidence for extreme
539 climatic events preceding the Triassic-Jurassic boundary: implications for the biotic crisis? GSA Bull., 120, 1408-1415,
540 2008.

541 Cohen, K. M., Finney, S. C., Gibbard, P. L., and Fan, J. X. The ICS International Chronostratigraphic Chart (2013 updated).
542 Episodes, 36, 199-204, 2013.

543 Cohen, A. S., Coe, A. L., Harding, S. M., and Schwark, L.: Osmium isotope evidence for the regulation of atmospheric CO₂
544 by continental weathering, Geology, 32, 157–160, 2004.

545 Crowley, T. J. and Berner, R. A.: CO₂ and climate change, Science, 292, 870–872, 2001.

546 Deng, S. H., Zhao, Y., Lu, Y. Z., Shang, P., Fan, R., Li, X., Dong, S. X., and Liu, L.: Plant fossils from the Lower Jurassic
547 coal-bearing formation of central InnerMongolia of China and their implications for palaeoclimate, Palaeoworld, 26:
548 279-316, 2017.

549 Dera, G., Brigaud, B., Monna, F., Laffont, R., Pucéat, E., Deconinck, J. F., Pellenard P., Joachimski, M. M., and Durllet, C.:
550 Climatic ups and downs in a disturbed Jurassic world, Geology, 39(3), 215-218, 2011.

551 Dera, G., Pellenard, P., Neige, P., Deconinck, J. F., Pucéat, E., and Dommergues, J. L.: Distribution of clay minerals in Early
552 Jurassic Peritethyan seas: Palaeoclimatic significance inferred from multiproxy comparisons, Palaeogeogr.
553 Palaeoclimatol. Palaeoecol., 271(1-2), 39–51, doi, 10.1016/j.palaeo.2008.09.010, 2009.

554 Dong, Z. M.: A new prosauropod from Ziliujing Formation of Sichuan Basin, Verte. Palasiatica, 22(4), 310-313, 1984 (in
555 Chinese with English abstract).

556 Duan, S. Y. and Chen, Y.: Mesozoic fossil plants and coal formation of eastern Sichuan Basin, in: Continental Mesozoic
557 Stratigraphy and Paleontology in Sichuan Basin of China: Part II, Paleontological Professional Papers, People's Publ.
558 House Sichuan, Chengdu, 491-519, 1982 (in Chinese).

559 Ekart, D. D., Cerling, T. E., Montñez, I. P., and Tabor, N. J.: A 400 million year carbon isotope record of pedogenic
560 carbonate: implications for paleoatmospheric carbon dioxide, Am. J. Sci., 299, 805-827, 1999.

561 Flügel, E.: Microfacies of Carbonate Rocks: Analysis, Interpretation and Application, Springer-Verlag, Berlin, Heidelberg,
562 New York, 976 pp. 2004.

563 Friedli, H., Lotscher, H., Oeschger, H., Siegenthale, U., and Stauffer, B.: Ice core record of the ¹³C/¹²C ratio of atmospheric
564 CO₂ in the past two centuries, Nature, 324, 237–238, 1986.

565 Fu, X. G., Wang, J., Feng, X. L., Wang, D., Chen, W. B., Song, C. Y., and Zeng, S. Q.: Early Jurassic carbon-isotope
566 excursion in the Qiangtang Basin (Tibet), the eastern Tethys: implications for the Toarcian Oceanic anoxic event, Chem.
567 Geol., 442, 67–72, 2016.

- 568 Gómez, J. J., and Goy, A.: Warming-driven mass extinction in the Early Toarcian (Early Jurassic) of northern Spain,
569 Correlation with other time-equivalent European sections. *Palaeogeogr. Palaeoclimatol. Palaeoecol.*, 306, 176-195,
570 2011.
- 571 Gómez, J. J., Comas-Rengifo, M. J., and Goy, A.: Palaeoclimatic oscillations in the Pliensbachian (Early Jurassic) of the
572 Asturian Basin (Northern Spain), *Clim. Past*, 12, 1199-1214, 2015.
- 573 Gómez, J. J., Goy, A., and Canales, M. L.: Seawater temperature and carbon isotope variations 15 in belemnites linked to
574 mass extinction during the Toarcian (Early Jurassic) in Central and Northern Spain. Comparison with other European
575 sections, *Palaeogeogr. Palaeoclimatol. Palaeoecol.*, 258, 28-58, 2008.
- 576 Guo, L. Y., Zhang, S. W., Xie, X. N., Li, Z. S., Huang, C. Y., and Chen, B. C.: Geochemical characteristics and organic
577 matter enrichment of the Dongyuemiao Member mudstone of Lower Jurassic in the Western Hubei-Eastern Chongqing,
578 *Ear. Sci.*, 42(7): 1235-1246, 2017 (in Chinese with English abstract).
- 579 Guo, Z. W., Deng, K. L., and Han, Y. H.: Formation and Evolution of the Sichuan Basin, Geo. Publ. House, Beijing, 200,
580 1996.
- 581 Hallam, A., and Wignall, P. B.: Mass extinctions and sea-level changes, *Earth Sci. Rev.*, 48, 217-250, 1999.
- 582 He, T. H. and Liao, C. F.: Control of Upper Triassic division and correlation and Indosinian Movement on oil and gas
583 accumulation in Sichuan Basin, *Acta Geol. Sichuan*, 00, 40-55, 1985 (in Chinese).
- 584 Hermoso, M., Le Callonnec, L., Minoletti, F., Renard, M., and Hesselbo, S. P.: Expression of the Early Toarcian negative
585 carbon-isotope excursion in separated carbonate microfrazctions (Jurassic, Paris Basin), *Earth Planet. Sci. Lett.*, 277,
586 194-203, 2009.
- 587 Hesselbo, S. P. and Jenkyns, H. C.: British Lower Jurassic sequence stratigraphy, in: *Mesozoic-Cenozoic Sequence*
588 *Stratigraphy of European Basins*, edited by: de Graciansky, P. C., Hardenbol, J., Jacquin, Th., and Vail, P. R., *SEPM*
589 *Spec. Pap.*, 60, 562-581, 1998.
- 590 Hesselbo, S. P., Gröcke, D. R., Jenkyns, H. C., Bjerrum, C. J., Farrimond, P., Morgans Bell, H. S., Green, O. R.: Massive
591 dissociation of gas hydrate during a Jurassic oceanic anoxic event, *Nature*, 406, 392-395, doi:10. 1038/35019044.,
592 2000.
- 593 Hesselbo, S. P., Jenkyns, H. C., Duarte, L. V., and Oliveira, L. C. V.: Carbon-isotope record of the Early Jurassic (Toarcian)
594 Oceanic Anoxic Event from fossil wood and marine carbonate Lusitanian Basin, Portugal, *Earth Planet. Sci. Lett.*, 253,
595 455-470, 2007.
- 596 Huang, P., Guan, Y. M., and Yang, X. Q.: Early Jurassic palynoflora from a drilling section of Jurong, Jiangsu, *Acta*
597 *Micropalaeontol. Sin.*, 17(1), 85- 98, 2000.
- 598 Huang, C. J., and Hesselbo, S. P.: Pacing of the Toarcian Oceanic Anoxic Event (Early Jurassic) from astronomical
599 correlation of marine sections. *Gondwana Res.*, 25, 1348-1356, doi, org/10.1016/j.gr.2013.06.023, 2014.

- 600 Huang, Q. S.: Paleoclimate and coal-forming characteristics of the Late Triassic Xujiahe stage in northern Sichuan, *Geol.*
601 *Rev.*, 41(1): 92–99, 1995, (in Chinese with English abstract).
- 602 Huang, Q. S.: The flora and paleoenvironment of the Early Jurassic Zhenzhuchong Formation in Daxian-Kaixian region,
603 northern margin of the Sichuan Basin, *Ear. Sci. J. China Uni. Geosci.*, 3, 221-229, 2001 (in Chinese with English
604 abstract).
- 605 Imbellone, P. A.: Classification of Paleosols. São Paulo, UNESP, *Geociências*, 30(1), 5-13, 2011,
- 606 Izumi, K., Kemp, D., Itamiya, S., and Inui, M.: Sedimentary evidence for enhanced hydrological cycling in response to rapid
607 carbon release during the early Toarcian oceanic anoxic event, *Earth Planet. Sci. Lett.*, 481, 162–170, 2018.
- 608 Jahren, A. H., Arens, N. C., and Harbeson, S. A.: Prediction of atmospheric $\delta^{13}\text{C}_{\text{CO}_2}$ using fossil plant tissues, *Rev. Geophys.*,
609 46, RG1002, doi: 10.1029/2006RG000219, 2008.
- 610 Jenkyns, H. C. and Clayton, C. J.: Black shales and carbon isotopes in pelagic sediments from the Tethyan Lower Jurassic,
611 *Sedimentology*, 33, 87-106, 1986.
- 612 Jenkyns, H. C., and Clayton, C. J., Lower Jurassic epicontinental carbonates and mudstones from England and Wales:
613 chemostratigraphic signals and the early Toarcian anoxic event, *Sedimentology*, 44, 687-706, 1997.
- 614 Jenkyns, H. C., Jones, C. E., Gröcke, D. R., Hesselbo, S. P., and Parkinson, D. N.: Chemostratigraphy of the Jurassic System:
615 Applications, limitations and implications for palaeoceanography, *J. Geol. Soc. London*, 159, 351-378, 2002.
- 616 Jenkyns, H. C.: Geochemistry of oceanic anoxic events, *Geochem. Geophys. Geosyst.*, 11, Q03004. doi:10.
617 1029/2009GC002788, 2010.
- 618 Jones, C. E., Jenkyns, H. C., and Hesselbo, S. P.: Strontium isotopes in Early Jurassic seawater: *Geoch. Cosmoch. Acta*, 58,
619 1285–1301, 1994.
- 620 Kemp, D. B., Coe, A. L., Cohen, A. S., and Schwark, L.: Astronomical pacing of methane release in the Early Jurassic
621 period, *Nature*, 437, 396-399, doi, org/10.1038/nature04037, 2005.
- 622 Kenny, R.: A cool time in the Early Jurassic: first continental palaeoclimate estimates from oxygen and hydrogen isotope
623 ratios in chert from Navajo Sandstone carbonate lenses, Utah (USA), *Carbonate Evaporite*, doi,
624 10.1007/s13146-015-0276-z, 2015.
- 625 Kent, D. V., Olsen, P. E., and Muttoni, G.: Astrochronostratigraphic polarity time scale (APTS) for the Late Triassic and
626 Early Jurassic from continental sediments and correlation with standard marine stages, *Earth-Sci. Rev.*, 166, 153-180,
627 2017.
- 628 Korte, C., and Hesselbo, S. P.: Shallow marine carbon and oxygen isotope and elemental records indicate
629 icehouse-greenhouse cycles during the Early Jurassic, *Paleoceanography*, 26, 1–18, 2011.
- 630 Korte, C., Hesselbo, S. P., Jenkyns, H. C., Rickaby, R. E. M., and Spötl, C.: Palaeoenvironmental significance of carbon-
631 and oxygen-isotope stratigraphy of marine Triassic-Jurassic boundary sections in SW Britain, *J. Geol. Soc. London*,

- 632 166(3), 431-445, 2009.
- 633 Korte, K., Hesselbo, S. P., Ullmann, C.V., Dietl, G., Ruhl, M., Schweigert, G., Thibault, N.: Jurassic climate mode governed
634 by ocean gateway, *Nat. Commun.*, 6, 10015, doi, 10.1038/ncomms10015, 2015.
- 635 Li, H. C. and Ku, T. L.: $\delta^{13}\text{C}$ - $\delta^{18}\text{O}$ covariance as a paleohydrological indicator for closed basin lakes, *Palaeogeogr.*
636 *Palaeoclimatol. Palaeoecol.*, 133, 69-80, 1997.
- 637 Li, L. Q., Wang, Y. D., Liu, Z. S., Zhou, N., and Wang, Y.: Late Triassic palaeoclimate and palaeoecosystem variations
638 inferred by palynological record in the northeastern Sichuan Basin, China, *Paläontol. Zeits.*, 309-324, DOI 10.
639 1007/s12542-016-0309-5, 2016.
- 640 Li, W. M. and Chen, J. S.: Discovery and significances of the Jurassic Ziliujing Formation in Tianzhu, Guizhou, China *New*
641 *Techn. Prod.*, 13, 134-135, 2010 (in Chinese).
- 642 Li, X. B. and Meng, F. S.: Discovery of fossil plants from the Ziliujing Formation in Hechuan of Chongqing. *Geol. Min.*
643 *Resour. South China*, 3: 60-65, 2003 (in Chinese with English abstract).
- 644 Li, Y. Q. and He, D. F.: Evolution of tectonic-depositional environment and prototype basins of the Early Jurassic in Sichuan
645 Basin and adjacent areas, *Acta Petrol. Sin.*, 35(2), 219-232, 2014 (in Chinese with English abstract).
- 646 Li, Y., Allen, P. A., Densmore, A. L., and Xu, Q.: Evolution of the Longmen Shan Foreland Basin (Western Sichuan, China)
647 during the Late Triassic Indosinian Orogeny. *Basin Res.*, 15, 117-138, 2003.
- 648 Liang, B., Wang, Q. W., and Kan, Z. Z.: Geochemistry of Early Jurassic mudrocks from Ziliujing Formation and
649 implications for source-area and weathering in dinosaur fossils site in Gongxian, Sichuan province, *J. Min. Petr.*, 26(3),
650 94-99, 2006 (in Chinese with English abstract).
- 651 Littler, K., Hesselbo, S. P., and Jenkyns, H. C.: A carbon-isotope perturbation at the Pliensbachian-Toarcian boundary:
652 evidence from the Lias Group, NE England. *Geol. Mag.*, 147, 181-192, 2010.
- 653 Liu, J. L., Ji, Y. L., Zhang, K. Y., Li, L. D., Wang, T. Y., Yang, Y., and Zhang, J.: Jurassic sedimentary system transition
654 and evolution model in western Sichuan Foreland Basin, *Acta Petrol. Sin.*, 37(6), 743-756, 2016 (in Chinese with
655 English abstract).
- 656 Ma, Y. S., Chen, H. D., Wang, G. L., Guo, T. L., Tian, J. C., Liu, W. J., Xu, X. S., Zheng, R. C., Mou, C. L., and Hou, M. C.:
657 Atlas of Lithofacies Paleogeography on the Sinian-Neogene Tectonic-Sequence in South China, Science Press, Beijing,
658 162-165, 2009 (in Chinese).
- 659 Mack, G. H. and James, W. C.: Paleoclimate and the Global Distribution of Paleosols, *J. Geol.*, 102, 360-366, 1994.
- 660 Mack, G. H., James, W. C., and Monger, H. C.: 1 Classification of paleosols, *Geol. Soc. Am. Bull.*, 105, 129-136, 1993.
- 661 McElwain, J. C., Wade-Murphy, J., and Hesselbo, S. P.: Changes in carbon dioxide during an oceanic anoxic event linked to
662 intrusion into Gondwana coals, *Nature*, 435, 479-482, doi:org/10. 1038/nature03618, 2005.
- 663 McKenzie, J. A., and Vasconcelos C.: Dolomite Mountains and the origin of the dolomite rock of which they mainly consist:

664 historical developments and new perspectives, *Sedimentology*, 56, 205 – 219, doi, 10.1111/j.1365-3091.2008.01027.x,
665 2009.

666 Meng, F. S., Chen, H. M., and Li, X. B.: Study on Lower Middle Jurassic boundary in Chongqing region, *Geol. Min. Resour.*
667 *S China*, 3, 64-71, 2005 (in Chinese with English abstract).

668 Meng, F. S., Li, X. B., and Chen, H. M.: Fossil plants from Dongyuemiao Member of the Ziliujing Formation and
669 Lower-Middle Jurassic boundary in Sichuan basin, China, *Acta Palaeontol. Sin.*, 42(4), 525-536, 2003. (in Chinese with
670 English abstract).

671 Metodiev, L. and Koleva-Rekalova, E.: Stable isotope records ($\delta^{18}\text{O}$ and $\delta^{13}\text{C}$) of Lower - Middle Jurassic belemnites from
672 the Western Balkan mountains (Bulgaria), *Palaeoenvironmental application, Appl. Geochem.*, 23, 2845–2856, 2008.

673 Mintz, J. S., Driese, S. G., Breecker, D. O., and Ludvigson, G. A.: Influence of changing hydrology on pedogenic calcite
674 precipitation in Vertisols, Dance Bayou, Brazoria County, Texas, USA: implications for estimating paleoatmospheric
675 $p\text{CO}_2$, *J. Sedi. Res.*, 81(6), 394-400, 2011.

676 Mo, Y. Z. and Yu, H. Y.: The discovery and its geological significance of dolomite in Ziliujing Groups of Middle and Lower
677 Jurassic Series in Ma'an shan Member, *Geol Guizhou*, 10(1), 110-113, 1987 (in Chinese with English abstract).

678 Montañez, I. P.: Modern soil system constraints on reconstructing deep-time atmospheric CO_2 , *Geochim. Cosmochim. Acta*,
679 101, 57–75, 2013.

680 Nadelhofer K. J., and Fry B.: Controls on natural nitrogen-15 and carbon-13 abundances in forest soil organic matter, *Soil*
681 *Sci. Soc. Am. J.*, 52, 1633-1640, 1988.

682 Newport, R., Hollis, C., Bodin, S., and Redfern, J.: Examining the interplay of climate and low amplitude sea-level change
683 on the distribution and volume of massive dolomitization: Zebbag Formation, Cretaceous, Southern Tunisia, *Deposit.*
684 *Rec.*, 3(1), 38–59, doi,10.1002/dep2.25, 2017.

685 Parrish, J. T., Hasiotis, S. T., and Chan, M. A.: Carbonate deposits in the Lower Jurassic Navajo Sandstone, southern Utah
686 and northern Arizona, *J. Sedi. Res.*, 87, 740-762, doi, <https://doi.org/10.2110/jsr.2017.42>, 2017.

687 Parrish, J. T., Rasbury, E. T., Chan, M. A., and Hasiotis, S. T.: Earliest Jurassic U-Pb ages from carbonate deposits in the
688 Navajo Sandstone, southeastern Utah, USA, *Geology*, 47(11), 1015–1019, doi, 10.1130/g46338.1, 2019.

689 Peng, G. Z.: Assemblage characters of Jurassic dinosaurian fauna in Zigong of Sichuan, *J. Geosci.*, 33(2), 113-123, 2009 (in
690 Chinese with English abstract).

691 Peti, L., Thibault, N., Clémence, M. E., Korte, C., Dommergues, J. L., Bougeault, C., Pellenard, P., Jelby, M. E., and
692 Ullmann, C. V.: Sinemurian-Pliensbachian Calcareous Nannofossil Biostratigraphy and Organic Carbon Isotope
693 Stratigraphy in the Paris Basin: Calibration to the Ammonite Biozonation of NW Europe, *Palaeogeogr. Palaeoclimatol.*
694 *Palaeoecol.*, 468, 142–161, 2017.

695 Petrash, D. A., Bialik, O. M., Bontognali, T. R. R., Vasconcelos, C., Roberts, J. A., McKenzie, J. A., and Konhauser, K. O.:

696 Microbially catalyzed dolomite formation: From near-surface to burial, *Earth Sci. Rev.*, 171, 558–582, doi,
697 10.1016/j.earscirev.2017.06.015, 2017.

698 Philippe M., Puijalon S., Suan G., Mousset S., Thévenard F., and Mattioli E.: The palaeolatitudinal distribution of fossil
699 wood genera as a proxy for European Jurassic terrestrial climate, *Palaeogeogr. Palaeoclimatol. Palaeoecol.*, 466, 373–
700 381, 2017.

701 Pole, M.: Vegetation and climate of the New Zealand Jurassic, *GFF*, 131:1-2, 105-111, DOI: 10. 1080/11035890902808948,
702 2009.

703 Price, G. D., Twitchett, R. J., Wheelley, J. R., and Buono, G.: Isotopic evidence for long term warmth in the Mesozoic, *Sci.*
704 *Rep.*, 3, 1438, doi, 10.1038/srep01438, 2013.

705 Qian, T., Liu, S. F., Wang, Z. X., Li, W. P., and Chen, X. L.: Characteristics of the Baitianba Formation conglomerate of
706 Lower Jurassic in the northern Sichuan basin and its constraint to the uplift of the south Dabashan, China *Sci. Paper*,
707 11(21), 2402-2408, 2016 (in Chinese with English abstract).

708 Rees, P. A., Zeigler, A. M., and Valdes, P. J.: Jurassic phytogeography and climates: new data and model comparisons, in:
709 *Warm Climates in Earth History*, edited by: Huber, B., MacLeod, K., and Wing, S., Cambridge University Press, 297–
710 318, 1999.

711 Retallack, G. J.: A 300-million-year record of atmospheric carbon dioxide from fossil plant cuticles, *Nature*, 411, 287-290,
712 2001a.

713 Retallack, G. J.: Adapting soil taxonomy for use with paleosols. *Quatern. Int.*, 51/52: 55-57, doi,
714 10.1016/S1040-6182(98)00039-1, 1998.

715 Retallack, G. J.: *Soils of the Past--An Introduction to Paleopedology*, Blackwell Science Ltd, Oxford, 333, 2001b.

716 Riding, J. B., Leng, M. J., Kender, S., Hesselbo, S. P., and Feist-Burkhardt, S.: Isotopic and palynological evidence for a new
717 Early Jurassic environmental perturbation, *Palaeogeogr. Palaeoclimatol. Palaeoecol.*, 374: 16–27, 2013.

718 Robinson, S. A., Andrews, J. E., Hesselbo, S. P., Radley, J. D., Dennis, P. F., Harding, I. C., and Allen, P.: Atmospheric
719 $p\text{CO}_2$ and depositional environment from stable-isotope geochemistry of calcrite nodules (Barremian, Lower
720 Cretaceous, Wealden Beds, England), *J. Geol. Soc., London*, 159, 215–24, 2002.

721 Robinson, S. A., Ruhl, M., Astley, D. L., Naafs, B. D. A., Farnsworth, A. J., Bown, P. R., Jenkyns, H. C., Lunt D. J.,
722 O'Brien, C., Pancost, R. D., and Markwick, P. J.: Early Jurassic North Atlantic sea-surface temperatures from TEX86
723 palaeothermometry. *Sedimentology*, 64(1), 215–230, doi, 10.1111/sed.12321, 2017.

724 Romanek, C., Grossman, E. and Morse, J.: Carbon isotopic fractionation in synthetic aragonite and calcite: effects of
725 temperature and precipitation rate, *Geochim. Cosmochim. Ac.*, 56, 419-430, 1992.

726 Rosales, I., Quesada, S., and Robles, S.: Primary and diagenetic isotopic signals in fossils and hemipelagic carbonates: the
727 Lower Jurassic of northern Spain, *Sedimentology*, 48, 1149–1169, 2001.

728 Royer, D. L.: CO₂-forced climate thresholds during the Phanerozoic: *Geochi. Cosmochi. Ac.*, 70, 56, 65–75, doi: 10.
729 1016/j.gca.2005.11.031, 2006.

730 Sabatino, N., Neri, R., Bellanca, A., Jenkyns, H., Baudin, F., Parisi, G., and Maseti, D.: Carbon isotope records of the Early
731 Jurassic (Toarcian) oceanic anoxic event from the Valdorbia (Umbria-Marche Apennines) and Monte Mangart (Julian
732 Alps) sections: palaeogeographic and stratigraphic implications, *Sedimentology*, 56, 1307-1328, 2009.

733 SBG (Sichuan Bureau of Geology): Reports of 1:200,000 Regional Geology Investigations (Profile Qianjiang), 48, 1975 (in
734 Chinese).

735 SBG (Sichuan Bureau of Geology): Reports of 1:200,000 Regional Geology Investigations (Profile Xuyong), 55, 1976 (in
736 Chinese).

737 SBG (Sichuan Bureau of Geology): Reports of 1:200,000 Regional Geology Investigations (Profiles Suining, Zigong,
738 Neijiang, Yibin, and Luzhou), 43-50, 1980a (in Chinese).

739 SBG (Sichuan Bureau of Geology): Reports of 1:200,000 Regional Geology Investigations (Profiles Yilong, Tongjiang,
740 Nanchong, Guang'an, and Chongqing), 100-101, 1980b (in Chinese).

741 SBGM (Sichuan Bureau of Geology and Mineral Resources): Geology of Sichuan Province, Geol. Publ. House, Beijing, 730,
742 1991 (in Chinese with English summary).

743 SBGM: Lithostratigraphy of Sichuan Province, China Uni. Geosci. Press, Wuhan, 388, 1997 (in Chinese).

744 Schaller, M. F., Wright, J. D., and Kent, D. V.: Atmospheric *p*CO₂ perturbations associated with the Central Atlantic
745 Magmatic Province, *Science*, 331, 1404-1409, doi, 10.1126/science.1199011, 2011.

746 Sellwood, B. W., and Valdes, P. J.: Jurassic climates, *P. Geologist Assoc.*, 119, 5-17, 2008.

747 Scotese, C. R.: Atlas of Jurassic Paleogeographic Maps, PALEOMAP Atlas for ArcGIS, volume 4, The Jurassic and Triassic,
748 Maps 32-42, Mollweide Projection, PALEOMAP Project, Evanston, IL, 2014.

749 Slater, S. M., Twitchett, R. J., Danise, S., and Vajda, V.: Substantial vegetation response to Early Jurassic global warming
750 with impacts on oceanic anoxia, *Nature Geo.*, doi, 10.1038/s41561-019-0349-z, 2019.

751 Soil survey Staff: Keys to Soil Taxonomy, Pocahontas Press, Blacksburg, VA, 1998.

752 Steinhorsdottir, M. and Vajda, V.: Early Jurassic (late Pliensbachian) CO₂ concentrations based 5 on stomatal analysis of
753 fossil conifer leaves from eastern Australia, *Gondwana Res.* 27, 829-897, 2015.

754 Storm, M. S., Hesselbo, S. P., Jenkyns, H. C., Ruhl, M., Ullmann, C. V., Xu, W., Leng, M. J., Riding, J. B., Gorbatenko, O.:
755 Orbital pacing and secular evolution of the Early Jurassic carbon cycle. *PNAS*, 117(8), 3974-3982, doi,
756 10.1073/pnas.1912094117, 2020.

757 Suan, G., Mattioli, E., Pittet, B., Lécuyer, C., Suchéras-Marx, B., Duarte, L. V., Philippe, M., Reggiani, L., and Martineau, F.:
758 Secular environmental precursors to Early Toarcian (Jurassic) extreme climate changes, *Earth Planet. Sci. Letts.*, 290,
759 448-458, doi, org/10. 016/j.epsl.2009.12.047, 2010.

760 Suan, G., Mattioli, E., Pittet, B., Mailliot, S., and Lécuyer, C.: Evidence for major environmental perturbation prior to and
761 during the Toarcian (Early Jurassic) oceanic anoxic event from the Lusitanian Basin, Portugal, *Paleoceanography*, 23,
762 PA1202, doi, org/10. 1029/2007PA001459, 2008.

763 Talbot, M. R.: A review of the palaeohydrological interpretation of carbon and oxygen isotopic ratios in primary lacustrine
764 carbonates. *Chem. Geol. (Isotope Geoscience Section)*, 80, 261-2791, 1990.

765 Tanner, L. H., and Lucas, S. The Whitmore Point Member of the Moenave Formation: Early Jurassic Dryland Lakes on the
766 Colorado Plateau, Southwestern USA, *Volum. Jur.*, 6(6), 11-21, 2008.

767 Tanner, L. H., Hubert, J. F., Coffey, B. P., and McNerney, D. P.: Stability of atmospheric CO₂ levels across the
768 Triassic/Jurassic boundary, *Nature*, 411, 675-677, 2001.

769 Them, TR, II, Gill, B. C., Caruthers, A. H., Gröcke, D. R., Tulskey, E. T., Martindale, R. C., Poulton, T. P., and Smit, P. L.:
770 High-resolution carbon isotope records of the Toarcian oceanic anoxic event (Early Jurassic) from North America and
771 implications for the global drivers of the Toarcian carbon cycle, *Earth Planet. Sci. Lett.*, 459, 118–126, 2017.

772 Tramoy, R., Schnyder, J., Nguyen, Tu T. T., Yans, J., Jacob, J., Sebilo, M., Derenne, S., Philippe, M., Huguet, A., Pons, D.,
773 and Baudin, F.: The Pliensbachian-Toarcian paleoclimate transition: New insights from organic geochemistry and C, H,
774 N isotopes in a continental section from Central Asia, *Palaeogeogr. Palaeoclimatol. Palaeoecol.*, 461, 310–327, 2016.

775 Tucker, M. E.: *Sedimentary rocks in the field - a practical guide* (4th ed.), Wiley-Blackwell, Chichester, England, 276 pp,
776 2011.

777 Vandeginste, V., and John, C. M.: Influence of climate and dolomite composition on dedolomitization: insights from a
778 multi-proxy study in the central Oman Mountains, *J. Sediment. Res.*, 82(3), 177-195, doi, 10.2110/jsr.2012.19, 2012.

779 van de Schootbrugge, B., Bachan, A., Suan, G., Richoz, S., Payne, J. L.: Microbes, mud, and methane: Cause and
780 consequence of recurrent Early Jurassic anoxia following the end-Triassic mass-extinction, *Palaeont.*, 56, 685-709,
781 2013.

782 van de Schootbrugge, B., Bailey, T. R., Katz, M. E., Wright, J. D., Rosenthal, Y., Feist-Burkhardt, S., and Falkowski, P. G.:
783 Early Jurassic climate change and the radiation of organic walled phytoplankton in the Tethys Sea, *Paleobiology*, 31,
784 73–97, 2005.

785 Vasconcelos, C., McKenzie, J. A., Bernasconi, S., Grujic, D., and Tien, A. J.: Microbial mediation as a possible mechanism
786 for natural dolomite formation at low temperatures, *Nature*, 377, 220–222, 1995.

787 Veizer, J., Godderis, Y., and François, L. M.: Evidence for decoupling of atmospheric CO₂ and global climate during the
788 Phanerozoic eon, *Nature*, 408, 698-701, 2000.

789 Wang, Q. W., Liang, B., Kan, Z. Z.: Carbon and oxygen isotopic compositions of lacustrine carbonates of the Early Jurassic
790 Ziliujing Formation in the Sichuan Basin and their paleolimnological significance, *J. Min. Petr.*, 26(2), 87-91, 2006 (in
791 Chinese with English abstract).

792 Wang, Y. D., Fu, B. H., Xie, X. P., Huang, Q. S., Li, K., Liu, Z. S., Yu, J. X., Pan, Y. H., Tian, N., and Jiang, Z. K.: The
793 Terrestrial Triassic and Jurassic Systems in the Sichuan Basin, China, in: Contributions to the 8th International Congress
794 odd the Jurassic System, edited by: Sha, J. G., Shi, X. Y., Zhou, Z. H., Wang, Y. D., Uni. Sci. Techn., China Press,
795 Hefei, Anhui, 1-136, 2010 (in Chinese).

796 Wang, Y. D., Mosbrugger, V., and Zhang, H.: Early to Middle Jurassic vegetation and climatic events in the Qaidam Basin,
797 Northwest China, *Palaeogeogr. Palaeoclimatol. Palaeoecol.*, 224, 200–216,
798 <http://dx.doi.org/10.1016/j.palaeo.2005.03.035>, 2005.

799 Warren, J.: Dolomite: occurrence, evolution and economically important associations, *Earth Sci. Rev.*, 52, 1–81, 2000.

800 Wei, M.: Continental Mesozoic Stratigraphy and Paleontology in the Sichuan Basin, People's Publ. House of Sichuan,
801 Chengdu, 346-363, 1982 (in Chinese with English summary).

802 Wen, W. and Zhao, B.: Stratigraphic character and sedimentary facies of the Ziliujing Formation in the Pujiang-Ya'An area,
803 Sichuan province, *J. Stratigr.*, 34(2), 219-224, 2010 (in Chinese with English abstract).

804 Wright, V. P.: Paleosol Recognition: A guide to early diagenesis in terrestrial settings (Chapter 12), in: Developments in
805 Sedimentology, edited by: Wolf K, H. and Chilingarian, G. V., 47, 591-619, 1992.

806 Xu, W. M., Ruhl, M., Jenkyns, H. C., Leng, M. J., Huggett, J. M., Minisini, D., Ullmann, C. V., Riding, J. B., Weijers, J. W.
807 H., Storm, M. S., Percival, L. M. E., Tosca, N. J., Idiz, E. F., Tegelaar, E. W., Hesselbo, S. P.: Evolution of the Toarcian
808 (Early Jurassic) carbon-cycle and global climatic controls on local sedimentary processes (Cardigan Bay Basin, UK),
809 *Earth Planet. Sci. Lett.*, 484, 396-411, 2018.

810 Xu, W. M., Ruhl, M., Jenkyns, H. C., Hesselbo, S. P., Riding, J. B., Selby, D., Naafs, B. D. A., Weijers, J. W. H., Pancost, R.
811 D., Tegelaar, E. W., and Idiz, E. F.: Carbon sequestration in an expanded lake system during the Toarcian oceanic
812 anoxic event, *Nat. Geosci.*, 129-135, doi, 10. 1038/NGEO2871, 2017.

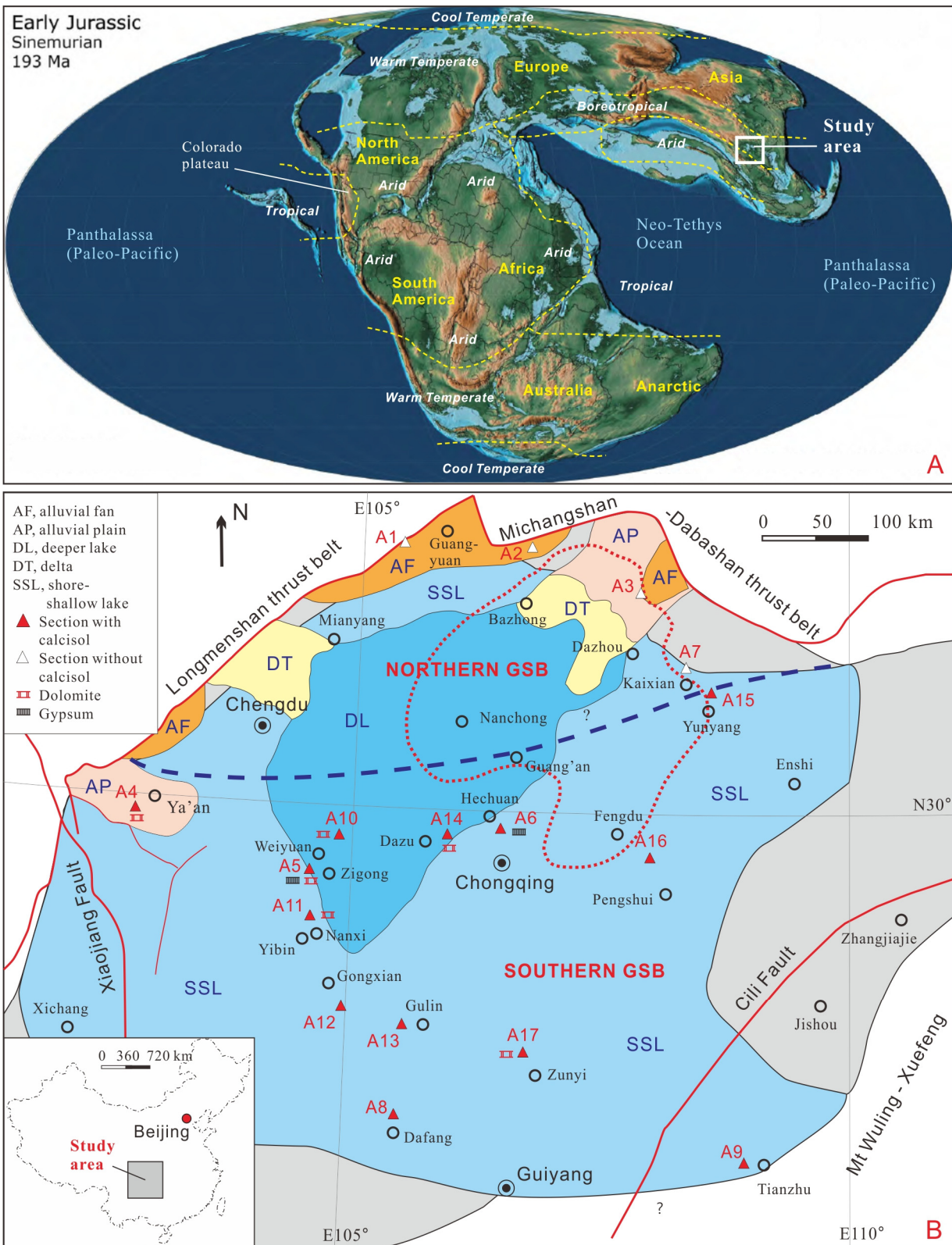
813 Yang, G. L.: Heavy mineral stratigraphy of Mesozoic continental clastic facies in Yaxi area, northern Guizhou, *J. Stratigr.*,
814 39(1), 89-96 , 2015 (in Chinese with English abstract).

815 Ye, M. N., Liu, X. Y., and Huang, G. Q.: Late Triassic and Early-Middle Jurassic fossil plants from northeastern Sichuan,
816 *Sci. Techn. Press. Hefei, Anhui*, 1986 (in Chinese with English summary).

817 Zhang, X. S., Zhao, B., Tan, M., Zhou, B. Y., Sun, J.: Stratigraphic Characteristics of Ziliujing Formation, Jurassic Series
818 and Discovery of Dinosaur Footprints in Dafang, Guizhou, *Geol. Guizhou*, 33(1), 50-70, 2016 (in Chinese with English
819 abstract).

820 Zhang, Z. L. and Meng, F. S.: Chapter 2, the Jurassic. In Zhang Zhenlai and Meng Fansong eds. The Triassic-Jurassic
821 Biostratigraphy in Yangtze Gorges (4), *Geol. Publ. House, Beijing*, 408, 1987 (in Chinese with English summary).

822



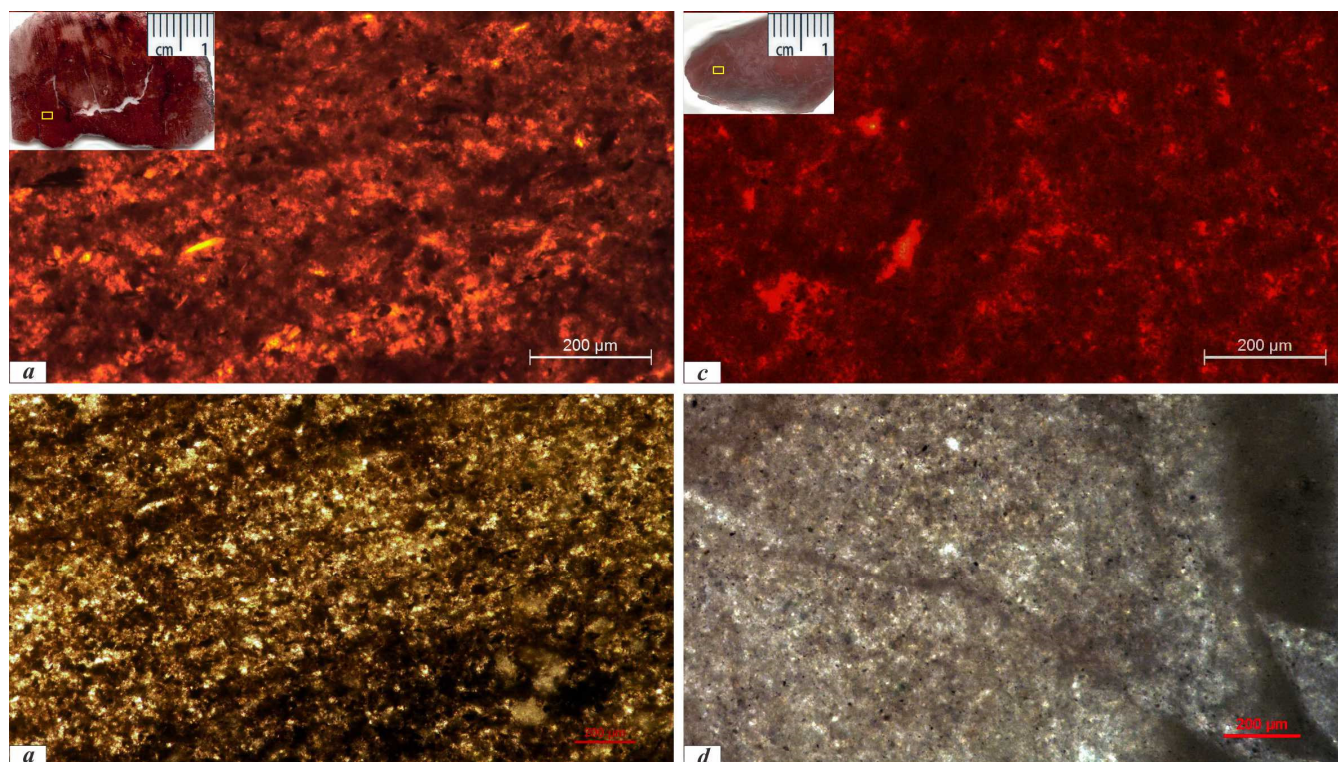
824

825 **Figure 1** A, Global Early-Middle Jurassic climate zones (Boucot et al., 2013) laid on the Early Jurassic (~193 Ma, Sinemurian)
 826 paleogeographic map (Scotese, 2014). B, Lithofacies paleogeographic sketch of the grand Sichuan paleobasin (GSB) in the early
 827 Early Jurassic (Zhenzhuchong and Dongyuemiao members) showing locations of the observed and analysed sections and
 828 climate-sensitive sediments. Lithofacies paleogeographic map was composed and modified from Ma et al. (2009) and Li and He
 829 (2014). Blue area is the extent of paleolake, estimated as ~380,000 km²; blue + gray region is the basin shape, estimated ~480,000
 830 km². Dot red line confines the deeper lake area in the late Early Jurassic (Ma'anshan and Da'anzhai members). Bold dashed line is

831 the northern edge of calcisol occurrence, which may separate the climate of the GSB as the northern and southern types. Triangles
832 with numbers are locations of observed and analysed sections: A1, Xiasi section, Jian'ge; A2, Puji section, Wangcang; A3,
833 Shiguansi section, Wanyuan; A4, Shaping section, Ya'an (bed and thickness from Wen and Zhao, 2010); A6, Tanba and Maliping
834 section, Hechuan (bed and thickness from Wang et al., 2010); A7, Wenquan section, Kaixian (thickness from Wang et al., 2010).
835 Location and source data of sections A5 and A8-A17 (climate-sensitive sediments) refer to supplementary data Table S1.

836

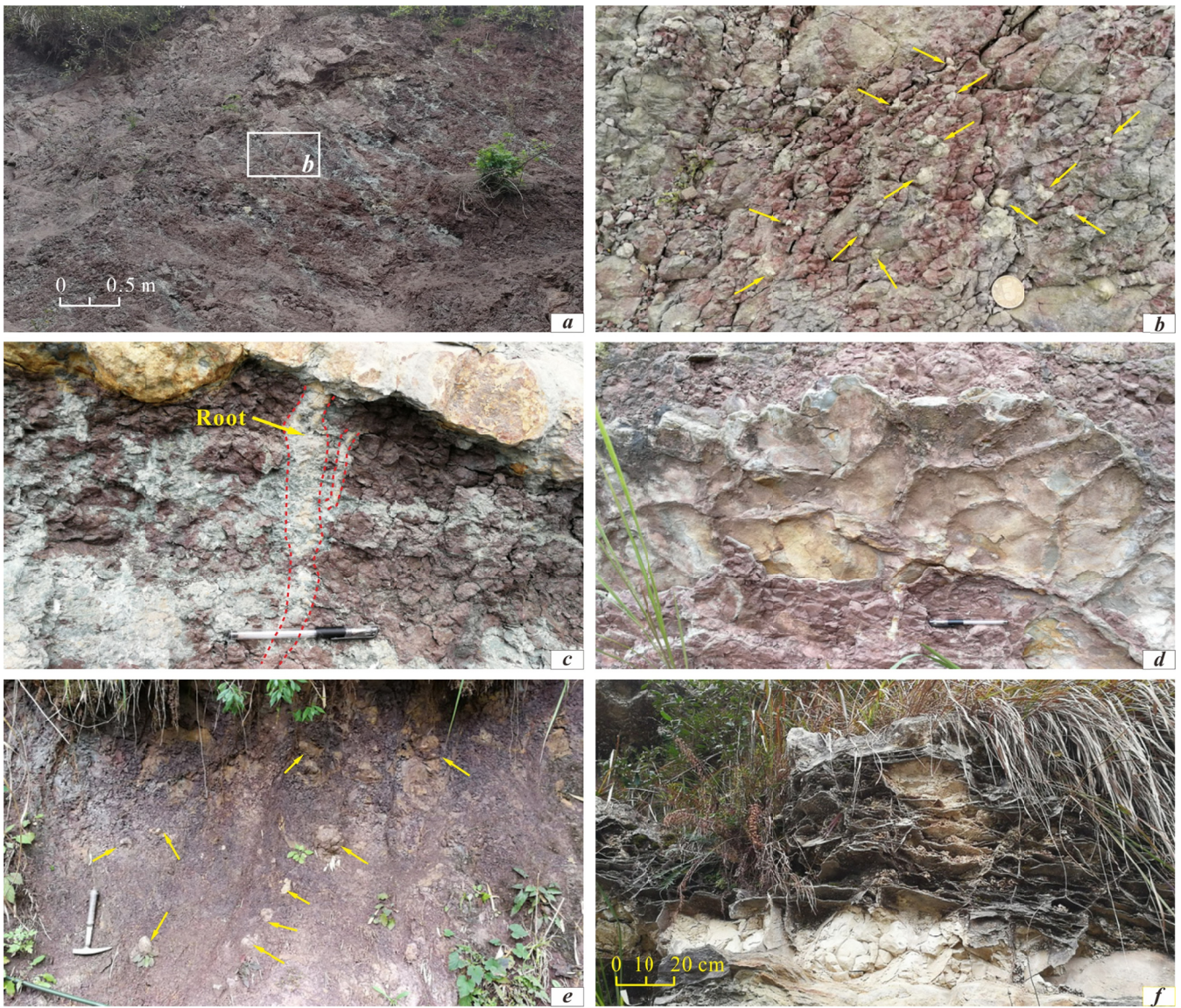
837



838

839 **Figure 2** Microscopic cathodoluminescence photos of representative calcrete samples from the Ziliujing Fm at the Shaping
840 section, Ya'an. *a*, Sample J_{1z}-12-01, Bed B12, Ma'anshan Member; *b*, Sample J_{1z}-22-01, Bed B22, Da'anzhai Member. Pedogenic
841 calcites are mainly null to non-luminescent, minor are orange/red luminescence. Inserts are the scanned photos of thin-section, and
842 rectangles are the area under cathodoluminescence and drilling.

843



844 **Figure 3** Field photographs of climate-sensitive sediments from the Lower Jurassic Ziliujing Fm in the GSB. *a*, Reddish purple
 845 calcisol with strong leaching structure. Lower Bed H8 of the upper Ma'anshan Member at Tanba, Hechuan. *b*, Reddish purple
 846 calcisol showing the density and size of calcretes. The horizon and location same as *a*. Arrows point to calcretes. Coin 2.0 cm in
 847 diameter. *c*, Reddish purple calcisol with strong leaching structure and rhizoliths. Bed H13 of the top Ma'anshan Member at
 848 Maliuping, Hechuna. Pen 15 cm long. *d*, Mudcracks. Lower Bed H8 of the upper Ma'anshan Member at Maliuping, Hechuan. Pen
 849 15 cm long. *e*, Brownish red calcisol with big calcretes (calcareous concretions). Arrows point to big calcretes. Calcisol horizon
 850 J_{1z}-10-01, Bed B10 of Ma'anshan Member at Shaping, Ya'an. Hammer 34 cm long. *f*, Chicken-wire structure. Bed H12 of the
 851 Da'anzhai Member at Maliuping, Hechuan.

852

853

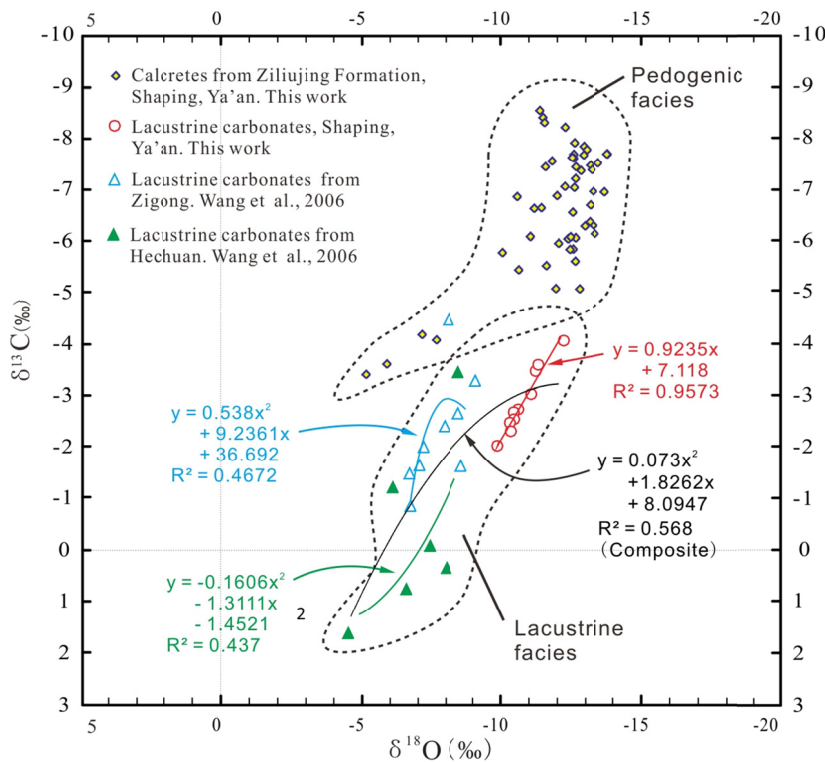
Series	Stage	Fm	Mem	A4	A10	A14	A6	A16	A15	A5	A11	A12	A13	A17	A8	A9	
174																	
(Ma)																	
176	Toa	Ziliujing?	Da'anzhai	West						East							
178																	
180																	
182.7	Pli	Ziliujing?	Ma'anshan														
190.8																	
194	Sin	Ziliujing?	Dongyue-mao														
196																	
198																	
199.3	Het	Ziliujing?	Zhengzhu-chong														
201.3																	
				Qijiang		Qijiang							Qijiang				

▭▭▭▭ Hiatus ▲ Calcisol □ Dolomitic sediment ▨ Gypsum?

854 **Figure 4** Diagram showing the temporal and spatial variation of climate-sensitive sediments in GSB. Section loactions and data
855 sources refer to Table S1.

856

857

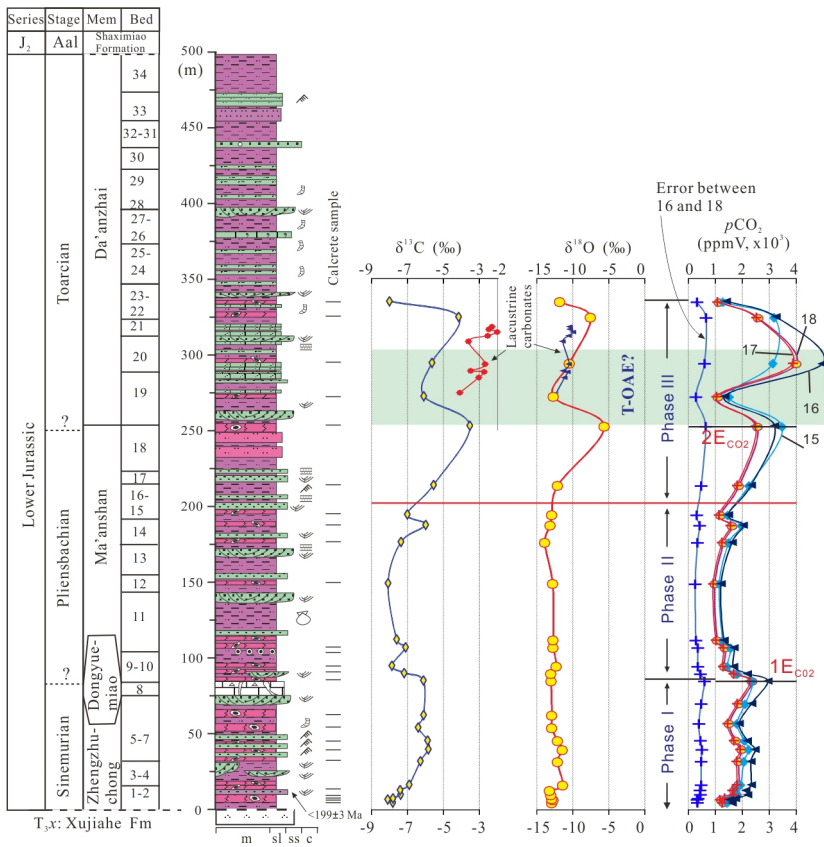


858 **Figure 5** Cross-plot and covariance of carbon and oxygen isotopic values of the Lower Jurassic pedogenic and lacustrine
859 carbonates from the GSB. Note, the pronounced covariance ($R^2=0.957$) between $\delta^{13}\text{C}$ and $\delta^{18}\text{O}$ from Shaping section, Ya'an,
860 indicating a compositional arid-evaporate and closed pattern lake; the moderate covariance ($R^2=0.47$ and 0.44) between $\delta^{13}\text{C}$ and
861 $\delta^{18}\text{O}$ from Zigong and Hechuan, indicating a (semi-) arid and semi-closed pattern lake.

862

863

864



865

866

867

868

869

870

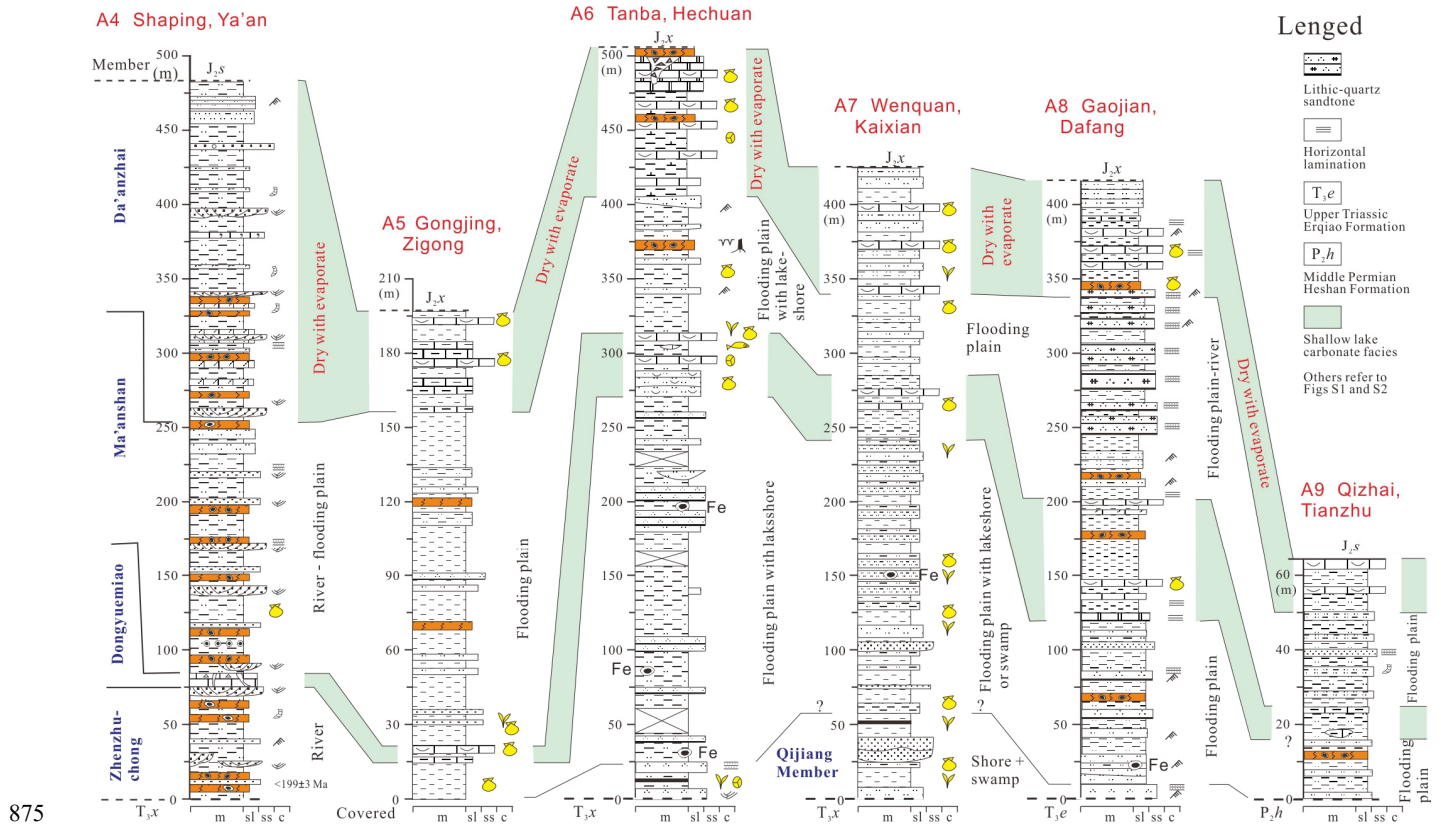
871

872

873

874

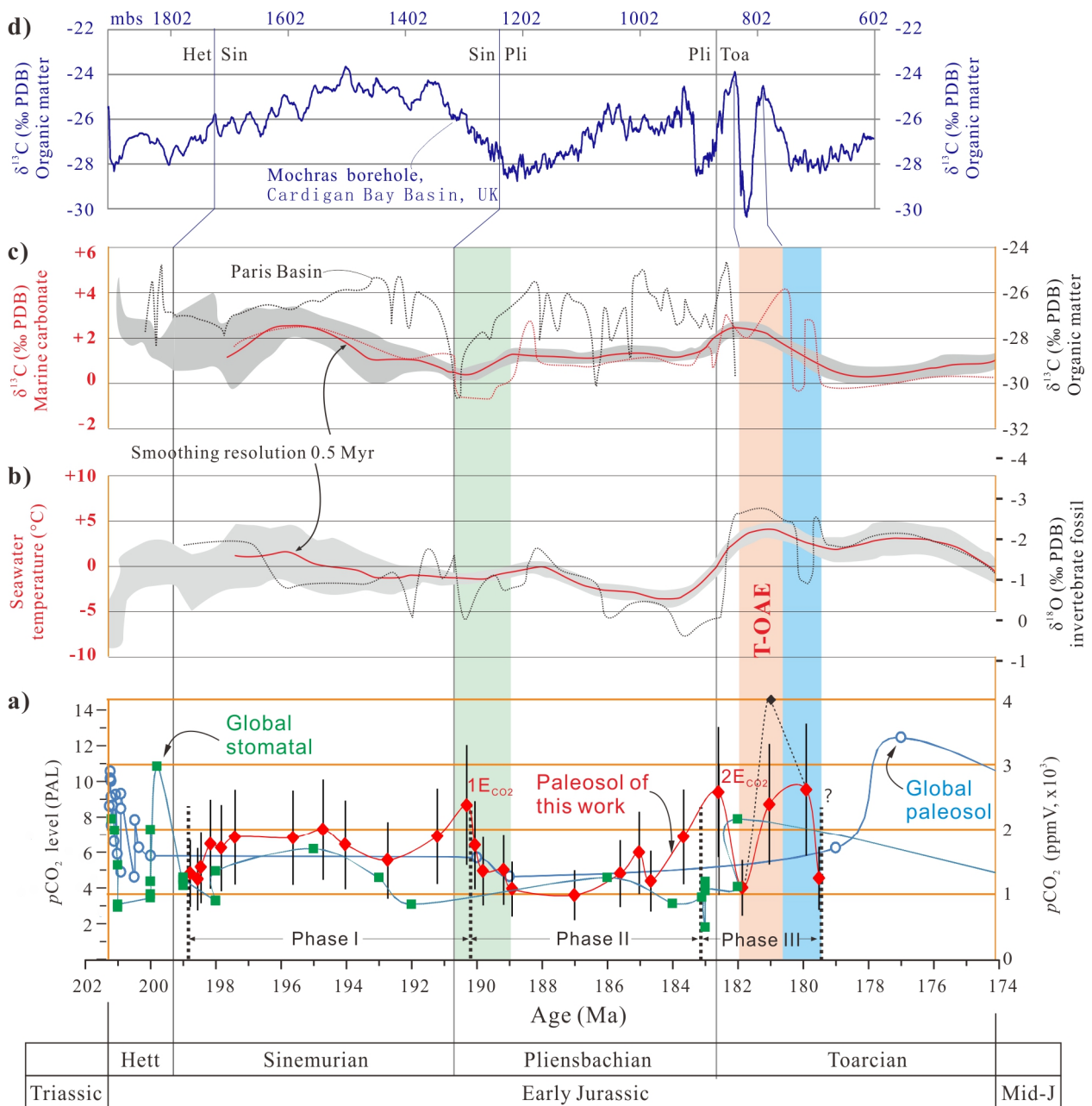
Figure 6 Diagram of the Lower Jurassic strata and lithological log at the Shaping section, Ya'an with carbon and oxygen isotope values of pedogenic and lacustrine carbonates and $p\text{CO}_2$ curve. Three phases and two events can be observed for both stable isotope values of pedogenic carbonates and $p\text{CO}_2$ estimate. Legend of lithology in log refers to supplementary Figs. S1 and S2. T-OAE, Toarcian oceanic anoxic event. 1E_{CO_2} and 2E_{CO_2} , rapid falling event of $p\text{CO}_2$. Numbers 15 to 18 are the curves of $p\text{CO}_2$ in different parameters, and details refer to supplementary Table S4. **Discrepancies (errors) are produced from the $p\text{CO}_2$ subtraction of column 16 (S_{O_2} =2500 ppmV) from column 18 (S_{O_2} =2000 ppmV) in Table S4, indicating that the largest uncertainty for the estimate of $p\text{CO}_2$ is the S_{O_2} . The highest difference of $p\text{CO}_2$ is 965 (3463-2498) ppmV (Sample J1Z-18-01 at depth 182.6 m), the lowest is 245 (1226-981) ppmV (Sample J1Z-12-01 at depth 148.9 m), and the mean is ~ 360 ppmV.**



875

876 **Figure 7 Stratigraphic correlation and depositional environment interpretation of the Lower Jurassic in the GSB. Data of**
 877 **sections refer to Fig. 1. Note, two lacustrine transgressive cycles are marked by correlative pale green areas.**

878



879 **Figure 8** Comparison among the Early Jurassic $p\text{CO}_2$, $\delta^{13}\text{C}$ of marine carbonates and organic matters, $\delta^{18}\text{O}$ of invertebrate
880 fossils, and seawater temperature. Age model is from Cohen et al. (2013). a), $p\text{CO}_2$ values of this work and the composite $p\text{CO}_2$ by
881 paleosol and stomatal index (supplementary Table S6 and S7). Vertical bars are errors (1σ) of $p\text{CO}_2$ (Table S5). Errors are
882 propagated using the Gaussian approach (Breecker and Retallack, 2014). Note: 1) $p\text{CO}_2 = 4027$ ppmV (black solid diamond,
883 sample J1z-20-01) if the $\delta^{13}\text{C}_r = -29.0$ ‰ at 181 Ma from Xu et al. (2018) in case of other constant parameters; 2) the early
884 published $p\text{CO}_2$ values from both carbon isotope of pedogenic carbonates and stomatal index of fossil plants (data refer to Table
885 S6 and S7) were awfully rough dated with the average age of a lithostratigraphic formation or group, with which the uncertainty
886 can be upto 10 Myr, leading to the difficulty of precise and accurate $p\text{CO}_2$ correlation in pace, frequency, and event. b), $\delta^{18}\text{O}$ and
887 seawater temperature (black dot line) of marine invertebrate fossils compiled from Rosales et al. (2001, 2004), Jenkyns et al. (2002),
888 Bailey et al. (2003), van de Schootbrugge et al. (2005), Gómez et al. (2008), Metodiev and Koleva-Rekalova (2008), Suan et al.
889 (2008), Korte et al. (2009), Dera et al. (2011), Gómez et al. (2015). c), red dot line $\delta^{13}\text{C}$ of marine carbonates in western Tethys,
890 composed from Jenkyns and Clayton (1986, 1997), Hesselbo et al. (2000), Dera et al. (2011), Arabas et al., 2017; black dot and solid
891 line $\delta^{13}\text{C}$ of organic matters from Paris Basin, France (Peti et al., 2017). Smoothed $\delta^{18}\text{O}$ and seawater temperature (red curves) in
892 b) and c) are after Dera et al. (2011). d), $\delta^{13}\text{C}$ of organic matters from North Atlantic. Composed from the Mochras borehole,
893 Cardigan Bay Basin, UK (Xu et al., 2018; Storm et al., 2020), seven-point average smoothing against depth (mbs).

894

896 **Table 1 Stratigraphic framework of the Lower Jurassic Ziliujing Fm in Sichuan and adjacent area (GSB), Southwest China**

Epoch	Age	Formation	W Sichuan (Ya'an)	E Sichuan and Chongqing	S Sichuan and N Guizhou	N Sichuan
Middle Jurassic	Aalenian	Xintiangou Fm	Xintiangou Fm	Xintiangou Fm	Xintiangou Fm	Qianfuyan / Xintiangou Fm
Early Jurassic	Toarcian	Ziliujing Fm	Da'anzhai Mem (Bed 20-34)	Da'anzhai Mem	Da'anzhai Mem	Baitianba Fm
	Pliensbachian		Ma'anshan Mem (Bed 9-18)	Ma'anshan Mem	Ma'anshan Mem	
	Sinemurian		Dongyuemiao Mem (Bed 8)	Dongyuemiao Mem	Dongyuemiao Mem	
			Zhenzhuchong Mem (Bed 1-7)	Zhenzhuchong Mem	Zhenzhuchong Mem	
	Hettangian		Hiatus	Qijiang Mem	Qijiang Mem	
Late Triassic	Rhaetian	Xujiahe Fm	Xujiahe Fm	Xujiahe Fm	Xujiahe Fm	

Notes: Straigraphic classification and correlation were composed from Dong (1984); SBGM (1997), Wang et al. (2010), Wen and Zhao (2010), Xu et al (2017). Re-Os isotope age of the lower Da'anzhai Member is 180.3 ± 3.2 Ma in western Sichuan (Xu et al., 2017). Fm, Formation; Mem, Member.

897

898 **Supplementary data**899 **Captions of supplementary figures**

900 **Figure S1 Lithological log of the Lower Jurassic Ziliujing Fm with depositional environment interpretations and sample**
 901 **positions at the Shaping section, Ya'an of Sichuan. Bed number and thickness are partly referred to Wen and Zhao (2010).**

902

903 **Figure S2 Lithological log of the Lower Jurassic Ziliujing Fm at the Tanba-Maliuping section, Hechuan of Chongqing with**
 904 **depositional environment interpretations and sample positions. Bed number and thickness are partly referred to Wang et al**
 905 **(2010).**

906

907 **Figure S3 Field photographs of the Lower Jurassic Ziliujing Fm lithofacies in the GSB. a, Well roundness and sorting gravels in**
 908 **the alluvial fan conglomerate. Basal and lower Baitianba Fm. Puji, Wangcang. Hammer 30 cm long. b, Large trough**
 909 **cross-bedding with scours in the point bar and channel sandstones. Upper Baitianba Fm; Puji, Wangcang. c, Calcisol developed**
 910 **within strong leaching overbank mudrocks on channelized sandstones. Middle of Bed B2, the Zhenzhuchong Member, Shaping**
 911 **section, Ya'an. d, Purple red mudrocks intercalated with thin siltstones in flood plain facies. Bed H7 of the Ma'anshan Member,**
 912 **Tanba section, Hechuan. e, Whitish medium-thick micritic dolomites in lacustrine facies. Bed H12 of the Da'anzhai Member,**
 913 **Maliuping section, Hechuan. Hammer 34 cm long. f, Greeinsh gray lacustrine muddy dolomites and dolomitic mudrocks**
 914 **associated with brownish / reddish purple mudrocks. Bed B21 of the Da'anzhai Member, Shaping section, Ya'an.**

915

916 **Figure S4 Microscopic photos showing lithological microfacies of the Lower Jurassic Ziliujing Fm. a, Fine lithic (quartz)**
 917 **sandstone. Lithic-dominant fragments are mudrock. Sample J_{1z}-02-01b, Zhenzhuchong Member, Shaping section, Ya'an.**
 918 **Plain-polarised light. b, Laminated muddy dolomite and dolomitic mudrocks. Sample J_{1z}-21S2B, Da'anzhai Member, Shaping**
 919 **section, Ya'an. Plain-polarised light. c, Fine quartz arenite. Sample 18HC-02b3, Bed H2, Qijiang Member, Tanba section,**
 920 **Hechuan. Cross-polarised light. d, Micritic dolomite. Sample 18HC-06b, Bed H12, Da'anzhai Member, Maliuping section,**
 921 **Hechuan. Plain-polarised light. e, Coquina. Shell wall of bivalves were micritized. Mud and recrystalline calcites filled inter-shells**

922 and intra-shells. Sample 18HC-04b, Base of Bed H12, Da'anzhai Member, Maliuping section, Hechuan. Cross-polarised light. *f*,
923 Relict of coquina. Shell wall of bivalves were partly micritized. Strongly recrystalline calcites replaced the fills and shells. Sample
924 18HC-05b, Bed H12, Da'anzhai Member, Maliuping section, Hechuan. Cross-polarised light.

925

926 **Figure S5** Field photographs of the Lower Jurassic Ziliujing Fm lithofacies in the GSB. *a*, Lithofacies and stratigraphic sequence.
927 Beds B8 to B10 of the lower Ma'anshan and Dongyuemiao members at Shaping, Ya'an. *b*, Karstified gravels within the limestone.
928 The horizon and location is same as *a*. Pen 15 cm long. *c*, Layered dolomites with Karstified cave gravels. Bed H12 of the
929 Da'anzhai Member at Maliuping, Hechuan. *d*, Karstified cave gravels. The horizon and location is same as *c*. Hammer 34 cm long.

930

931 **Figure S6** Stratigraphic correlation of the Lower Jurassic Baitianba Fm in northern GSB. Locations and sources refer to Figure
932 1. Plant fossils and stratal thickness in the Shiguansi section, Wanyuan are cited from SBG (1980b).

933

934 Captions of supplementary tables

935 **Table S1** Occurrence list of the Early Jurassic climate-sensitive sediments in the GSB

936

937 **Table S2** Early Jurassic paleosols in Ya'an of Sichuan and Hechuan of Chongqing, Southwest China

938

939 **Table S3** Carbon-oxygen isotope composition of lacustrine carbonates from the Lower Jurassic Ziliujing Fm (Da'anzhai Mem) in
940 the GSB

941

942 **Table S4** $p\text{CO}_2$ estimate by carbon isotope of pedogenic carbonates from the Lower Jurassic Ziliujing Fm at Shaping, Ya'an
943 of Sichuan

944

945 **Table S5** Calculation of $p\text{CO}_2$ and Gaussian error propagation using the atmosphere determination of global organic matter
946 isotope composition for the Early Jurassic Sichuan paleobasin

947

948 **Table S6** Global $p\text{CO}_2$ data of the Latest Triassic - Early Jurassic by stomatal method

949

950 **Table S7** Global $p\text{CO}_2$ data of the Latest Triassic - Early Jurassic estimated by carbon isotope of pedogenic carbonates

951

952 **Table S8** Calculation of $p\text{CO}_2$ and Gaussian error propagation using the atmosphere carbon isotope determination of marine
953 fossil carbonate carbon isotope composition for the Early Jurassic Sichuan paleobasin

954 Captions of supplementary notes

955 **Note S1**, Description and interpretation of sedimentary facies and its evolution

956

957